










RESEARCH ARTICLE

10.1029/2022JA031206

Global Hall MHD Simulations of Mercury's Magnetopause Dynamics and FTEs Under Different Solar Wind and IMF Conditions

Changkun Li¹ , Xianzhe Jia¹ , Yuxi Chen² , Gabor Toth¹, Hongyang Zhou³ , James A. Slavin¹ , Weijie Sun¹ , and Gangkai Poh⁴ 

¹Department of Climate and Space Sciences and Engineering, University of Michigan – Ann Arbor, Ann Arbor, MI, USA,

²Princeton University, Princeton, NJ, USA, ³University of Helsinki, Helsinki, Finland, ⁴NASA Goddard Space Flight Center, Greenbelt, MD, USA

Key Points:

- 3D global Hall magnetohydrodynamics simulations and an automated identification algorithm are developed to study flux transfer event formation and associated dynamics at Mercury
- Properties of simulated FTEs agree well with MErcury Surface Space ENvironment, GEOchemistry, and Ranging (MESSENGER) observations and exhibit clear dependence on solar wind M_A and interplanetary magnetic field orientation
- FTEs make a significant contribution to the open flux generation in Mercury's magnetosphere, consistent with previous MESSENGER findings

Correspondence to:

C. Li,
changkul@umich.edu

Citation:

Li, C., Jia, X., Chen, Y., Toth, G., Zhou, H., Slavin, J. A., et al. (2023). Global Hall MHD simulations of Mercury's magnetopause dynamics and FTEs under different solar wind and IMF conditions. *Journal of Geophysical Research: Space Physics*, 128, e2022JA031206. <https://doi.org/10.1029/2022JA031206>

Received 6 DEC 2022

Accepted 20 APR 2023

Abstract Mercury possesses a miniature but dynamic magnetosphere driven primarily by the solar wind through magnetic reconnection. A prominent feature of the dayside magnetopause reconnection that has been frequently observed is flux transfer events (FTEs), which are thought to be an important player in driving the global convection at Mercury. Using the BATSUS Hall magnetohydrodynamics model with coupled planetary interior, we have conducted a series of global simulations to investigate the generation and characteristics of FTEs under different solar wind Alfvénic Mach numbers (M_A) and interplanetary magnetic field (IMF) orientations. An automated algorithm was also developed to consistently identify FTEs and extract their key properties from the simulations. In all simulations driven by steady upstream conditions, FTEs are formed quasi-periodically with recurrence time ranging from 2 to 9 s, and their characteristics vary in time as they evolve and interact with the surrounding plasma and magnetic field. Our statistical analysis of the simulated FTEs reveals that the key properties of FTEs, including spatial size, traveling speed and core field strength, all exhibit notable dependence on the solar wind M_A and IMF orientation, and the trends identified from the simulations are generally consistent with previous MErcury Surface Space ENvironment, GEOchemistry, and Ranging observations. It is also found that FTEs formed in the simulations contribute about 3%–13% of the total open flux created at the dayside magnetopause that participates in the global circulation, suggesting that FTEs indeed play an important role in driving the Dungey cycle at Mercury.

1. Introduction

Mercury, the innermost planet in the solar system, has a very dynamic magnetosphere due to its proximity to the Sun. With its relatively weak intrinsic field and absence of notable rotational effects, Mercury's magnetosphere is often considered a scaled-down version of the terrestrial magnetosphere in that its global magnetospheric convection and dynamics are predominantly driven by the solar wind through magnetic reconnection (e.g., J. A. Slavin & Holzer, 1979). Since the arrival of MErcury Surface Space ENvironment, GEOchemistry, and Ranging (MESSENGER) at Mercury, numerous studies have examined the in-situ data from MESSENGER to investigate reconnection-driven dynamics in Mercury's magnetosphere. For example, DiBraccio et al. (2013) and J. A. Slavin et al. (2009, 2010) found that shocked IMF can reconnect with Mercury's intrinsic field under a wide range of shear angles and the resultant reconnection rate appears to be larger than those typically observed at the magnetopauses of Earth and other magnetized planets. Intense, frequent magnetopause reconnection combined with the small system size of the magnetosphere lead to a rapid Dungey cycle at Mercury, whose duration is of the order of a couple of minutes (J. A. Slavin et al., 2010), much shorter than the typical duration of ~60 min at Earth (Baker et al., 1996).

One of the key products of magnetopause reconnection is flux transfer events (FTEs), which were first discovered at the Earth's magnetopause based on magnetic field measurements (Russell & Elphic, 1978). FTEs are typically characterized by bipolar variations in the magnetic field component normal to the magnetopause surface and enhanced field strength near the center of the structure. Such magnetic signatures associated with FTEs suggest that their interior structures mostly resemble magnetic flux ropes with helical topology. As revealed by MESSENGER observations, FTEs are prevalent at Mercury and consequently considered an important player in driving Mercury's magnetospheric dynamics (e.g., J. A. Slavin et al., 2010) and influencing Mercury's exosphere through enhanced surface sputtering (e.g., W. Sun et al., 2022). In this work, we define

©2023. The Authors.

This is an open access article under the terms of the [Creative Commons Attribution License](https://creativecommons.org/licenses/by/4.0/), which permits use, distribution and reproduction in any medium, provided the original work is properly cited.

“FTEs” as flux ropes developing in the magnetopause current layer as a result of multiple X -line reconnection. The helical magnetic flux making up the FTE are “open” with one end connected to the draped IMF and the other end rooted in Mercury. The additional magnetic flux opened by magnetopause reconnection also fills the regions between the individual flux ropes and helps to pull them away from the quasi-stagnant subsolar regions and toward the cusp and into the outer layers of the northern and southern magnetic lobes of the tail. The total magnetic flux opened by dayside reconnection is therefore the sum of these two sources (e.g., W. J. Sun et al., 2020b). The study by J. A. Slavin et al. (2012) showed that the time separation between consecutive FTEs can be as brief as only a few seconds, much shorter than typically observed for Earth’s FTEs, which is of the order of minutes. The frequent occurrence of FTEs observed at Mercury has motivated a number of observational and theoretical studies to assess the role of FTEs in driving the global convection in Mercury’s magnetosphere. In particular, Imber et al. (2014) carried out a case study of large-size FTEs observed by MESSENGER and estimated that large FTEs could carry at least 30% of the open flux needed to drive the substorm cycle at Mercury. W. J. Sun et al. (2020) recently conducted a comprehensive survey of FTE showers observed by MESSENGER, which correspond to clusters of relatively small-size FTEs, and inferred that during FTE shower intervals, FTEs can carry 60%–85% of the open magnetic flux involved in driving Mercury’s Dungey cycle. Drawing an analogy with Earth’s FTEs, Fear et al. (2019) argued that the amount of magnetic flux opened by FTEs may represent an even greater contribution if one also takes into account the magnetic flux contained in the post-FTE reconnection exhaust. All of those previous works point to the idea that FTEs could be a major contributor in producing the open flux needed to drive Mercury’s Dungey cycle, which is in sharp contrast with the situation at other planetary magnetospheres, such as those of Earth, Jupiter and Saturn. However, the in-situ measurements available at Mercury, such as those from MESSENGER, were all obtained from single-point observations with limited spatial coverage. As a result, it remains a challenge to develop quantitative understanding of how magnetopause reconnection occurs and its impact on the global dynamics solely based on single spacecraft observations.

Global simulations based on various modeling approaches, including magnetohydrodynamics (MHD) (e.g., Jia et al., 2015; Kabin et al., 2008), hybrid (e.g., Exner et al., 2018; Fatemi et al., 2018; Müller et al., 2012; Trávníček et al., 2010), coupled fluid-kinetic (Chen et al., 2019) and fully kinetic (Lapenta et al., 2022; Lavorenti et al., 2022) models, have been applied to Mercury’s magnetosphere to obtain global context that is not readily available from in-situ observations. Most previous simulation studies have focused on the large-scale configuration and global-scale dynamics of the magnetosphere, and, as such, there have not been many modeling efforts devoted to FTEs at Mercury. It is only recently that a hybrid simulation was conducted by Lu et al. (2022) to investigate FTE formation for two IMF configurations (purely northward and purely southward orientation). However, many outstanding questions still remain unanswered regarding FTEs at Mercury, such as their 3D structure, time evolution and overall contribution to the global dynamics as well as how those FTE characteristics vary depending on the external conditions. A systematic modeling study is warranted in order to obtain global context for addressing those open questions related to Mercury’s FTEs.

In this work, we employ the BATS-R-US global Hall MHD model (Tóth et al., 2008) to simulate Mercury’s magnetosphere with a focus on understanding the generation and characteristics of FTEs under a variety of solar wind and IMF conditions. As demonstrated by previous numerical studies (e.g., Birn et al., 2001; Liu et al., 2022), by allowing separate bulk motions of plasma ions and electrons Hall-MHD is capable of producing fast reconnection with reconnection rates comparable to those seen in fully kinetic simulations and it is also computationally cheaper compared to fully kinetic models. These properties make Hall-MHD a suitable tool for our modeling study, in which we aim to conduct multiple simulations to systematically investigate the effects of different upstream conditions on FTEs. The external parameters we focus on in this work are the solar wind Alfvénic Mach number and the IMF orientation, which have been found through MESSENGER observations to have significant influences on Mercury’s FTEs (e.g., W. J. Sun et al., 2020b).

The details of our numerical model, simulation setup and input parameters are described in Section 2. Section 3 introduces an automated algorithm that we have developed to automatically identify FTEs in our simulations as well as various analysis techniques used to extract key FTE properties from the model. Results of the simulated FTEs, including their physical properties and statistics, are also presented in Section 3 and further discussed in Section 4. Section 5 provides a summary and conclusions.

2. Methodology

In this work, the interaction between Mercury's magnetosphere and the solar wind is simulated using a 3D global Hall-MHD model based on the BATSRUS (Block Adaptive Tree Solar wind Roe-type Upwind Scheme) code (Powell et al., 1999). BATSRUS is a high-performance magnetohydrodynamic code that uses a variety of numerical schemes to solve the MHD equations of different forms (e.g., ideal, Hall, multi-fluid, etc.) BATSRUS itself is also a component of the Space Weather Modeling Framework (SWMF), which was developed to provide a comprehensive physics-based description of space weather conditions in different environments, including the Sun and various planetary bodies (e.g., Gombosi et al., 2021; Tóth et al., 2012). The BATSRUS Hall MHD model is described in detail in Tóth et al. (2008). Here, we focus on the key aspects of the simulation model adapted for Mercury, including the set of equations solved, the model configuration and the structure of the numerical grid specifically designed to capture the dayside magnetopause dynamics.

Equations 1–7 describe the full set of equations solved in our Hall MHD model, where the primitive variables are plasma mass density, plasma bulk velocity (which is approximately the ion bulk velocity), magnetic field, ion pressure and electron pressure (ρ , u , B , p , p_e). Other derived quantities include the current density, $j = \nabla \times B/\mu_0$, and the electron bulk velocity $u_e = u - j/ne$, where n is the plasma number density. In Equation 7, e represents the total energy density, which is the sum of the hydrodynamic energy density and the magnetic energy density, and γ is the ratio of specific heats set to be 5/3.

$$\frac{\partial \rho}{\partial t} = -\nabla \cdot (\rho \mathbf{u}) \quad (1)$$

$$\frac{\partial (\rho \mathbf{u})}{\partial t} = -\nabla \cdot \left(\rho \mathbf{u} \mathbf{u} + (p + p_e) \mathbf{I} + \frac{B^2}{2\mu_0} \mathbf{I} - \frac{B\mathbf{B}}{\mu_0} \right) \quad (2)$$

$$\frac{\partial e}{\partial t} = -\nabla \cdot \left[(\varepsilon + p) \mathbf{u} + (\varepsilon_e + p_e) \mathbf{u}_e + \mathbf{u}_e \cdot \left(\frac{B^2}{\mu_0} \mathbf{I} - \frac{B\mathbf{B}}{\mu_0} \right) - B \times \eta \mathbf{j} \right] \quad (3)$$

$$\frac{\partial \mathbf{B}}{\partial t} = -\nabla \times \left[\mathbf{u} \times \mathbf{B} - \frac{\mathbf{j}}{ne} \times \mathbf{B} + \eta \mathbf{j} + \frac{\nabla p_e}{ne} \right] \quad (4)$$

$$\frac{\partial p_e}{\partial t} + \nabla \cdot (p_e \mathbf{u}_e) = -(\gamma - 1) p_e \nabla \cdot \mathbf{u}_e \quad (5)$$

$$\mathbf{u}_e = \mathbf{u} - \frac{\mathbf{j}}{ne} \quad (6)$$

$$e = \frac{1}{2} \rho \mathbf{u}^2 + \frac{1}{\gamma - 1} p + p_e + \frac{B^2}{2\mu_0} \quad (7)$$

To solve the set of MHD equations above, we have used a second-order finite-volume scheme with a Harten–Lax–van Leer–Einfeldt Riemann solver (Einfeldt et al., 1991) and Koren's third-order limiter (Koren, 1993). The time stepping is done in a semi-implicit manner where the resistive term $\eta \mathbf{j}$ and the Hall term $-(\mathbf{j} \times \mathbf{B})/(ne)$ in the induction equation (Equation 4) are advanced with an implicit scheme, whereas all the other terms are advanced using explicit time stepping (Tóth et al., 2012). The advantage of using a semi-implicit scheme is that it helps to reduce the stiffness of the system without limiting the time step of the explicit time-stepping, thereby allowing us to achieve affordable computational costs for running multiple global Hall-MHD simulations. To maintain the divergence-free property of the magnetic field, we have combined the eight-wave scheme and the hyperbolic cleaning scheme to remove excess $\nabla \cdot \mathbf{B}$ from the simulation domain (Tóth, 2000).

The simulation domain covers a rectangular box with dimensions of $-64 R_M < X < 8 R_M$, $-128 R_M < Y < 128 R_M$, $-128 R_M < Z < 128 R_M$, where $R_M = 2440$ km is Mercury's mean radius. Here, X , Y , Z are defined in Mercury Solar Orbital (MSO) coordinates, where the $+X$ -axis is pointing from Mercury to the Sun, the $+Z$ -axis is perpendicular to Mercury's equatorial plane and is pointing northward, and the Y -axis completes the right-handed system with positive pointing in the direction opposite to Mercury's orbital motion. A Hall factor of 4 has been multiplied to the plasma ion mass-to-charge ratio in the MHD equations, which in effect scales up the ion inertial length by a factor of 4. As shown by Tóth et al. (2017), scaling the ion kinetic scale length using this approach results

Table 1
Solar Wind and Interplanetary Magnetic Field (IMF) Parameters for the Simulations Presented in This Study

Run #	M_A	IMF clock angle (°)	B_y (nT)	B_z (nT)	U_x (km/s)	ρ (amu/cc)	T (K)
1	6	180	0	-23	-500	36	8.7e4
2	6	135	-16	-16	-500	36	8.7e4
3	6	90	-23	0	-500	36	8.7e4
4	2	180	0	-69	-500	36	8.7e4
5	2	135	-49	-49	-500	36	8.7e4
6	2	90	-69	0	-500	36	8.7e4

in considerable reduction in the computational costs required to resolve the ion kinetic physics without significantly changing the behavior of the global simulation provided that the scaled ion inertial length is still well separated from the global scale, which is the case here for Mercury. We have used a stretched spherical grid with up to three levels of adaptive mesh refinement near the dayside magnetopause, resulting in a grid resolution of 20 km (or $0.008 R_M$), which is about one sixth of the effective ion inertial length (d_i) at the magnetopause after scaling. Such a high grid resolution ensures that the ion scale physics is well resolved in our simulations.

A key difference of this modeling work from the previous MHD simulations of Mercury's magnetosphere is the use of Hall-MHD, which has been shown to be able to enable fast reconnection with reconnection rates comparable to those seen in fully kinetic simulations (e.g., Birn et al., 2001; Liu et al., 2022). The Hall term in the induction equation (Equation 4) becomes

important only in regions of strong electric currents, which, in Mercury's case, lie in the magnetopause and magnetotail regions. Therefore, we have chosen to turn on the Hall term in a rectangular box ($-8 R_M < X < 2 R_M$, $-4 R_M < Y < 4 R_M$, $-4 R_M < Z < 4 R_M$) that covers the entire dayside magnetosphere and the majority of the nightside magnetotail. To save computational costs, the Hall term is switched off outside this box and inside the sphere of radius of $1.15 R_M$ where there are no significant plasma currents (and hence the Hall effect) present.

Mercury possesses a large-size conducting core with a radius of $\sim 0.8 R_M$, which has been shown to play an important role in governing the structure of Mercury's magnetosphere (e.g., Heyner et al., 2016; Jia et al., 2015, 2019; J. A. Slavin et al., 2014; J. Slavin et al., 2019). To account for the induction effect of Mercury's conducting core, we have followed the approach used in previous Mercury simulations by Jia et al. (2015, 2019) to include Mercury's interior in our global Hall-MHD simulations. Specifically, the planetary interior is assumed to consist of a conducting core of radius $0.8 R_M$ and a resistive mantle (between 0.8 and $1.0 R_M$) characterized by a prescribed resistivity profile according to Jia et al. (2015). For the interior, the MHD primitive variables (except the magnetic field) are set to constants and only the magnetic field is solved for and updated inside Mercury's interior using the induction equation that allows the magnetic field to diffuse in time into the planet according to the prescribed resistivity profile. At the core-mantle boundary ($r = 0.8 R_M$), we apply a zero magnetic field perturbation boundary condition so that below this boundary the magnetic field is fixed to Mercury's intrinsic field, which is represented as a dipole aligned with the Z -axis with an equatorial surface strength of 195 nT and a northward offset of $0.2 R_M$ (Anderson et al., 2011). Outside of the planet ($r > 1.0 R_M$) the full set of MHD equations described above are solved, and, therefore, boundary conditions need to be prescribed at the planet's surface for the plasma density, velocity and pressure. For the plasma ion and electron pressure, we apply a floating boundary condition, that is the values in the ghost cell are set to be equal to those in the physical cell inside the simulation domain ($p_{\text{ghost}} = p_{\text{physical}}$). In terms of the plasma density, we apply different treatments based on the direction of the plasma bulk velocity in the physical cell right next to the boundary: (a) if the plasma is flowing toward the surface, then we apply a floating boundary condition $\rho_{\text{ghost}} = \rho_{\text{physical}}$, which allows the incoming plasma to be absorbed by the surface; (b) if the plasma flow has a radially outward component, then we fix the plasma density to a relatively small value, $\rho_{\text{ghost}} = 5$ amu/cc. For the simulations presented in this work, the total source rate of outflowing plasma from the surface boundary into the magnetosphere ranges between $1 - 6 \times 10^{24}$ amu/s, consistent with the idea that Mercury's surface acts as a very weak source of plasma (e.g., Raines et al., 2015). Finally, we use a magnetic field-based boundary condition to set the plasma velocity in the ghost cell in which the parallel component of velocity with respect to magnetic field in physical cell is reversed ($\mathbf{u}_{\text{ghost}} \cdot \mathbf{B} = -\mathbf{u}_{\text{physical}} \cdot \mathbf{B}$) from the parallel component in the physical cell and the perpendicular component is kept the same ($\mathbf{u}_{\text{ghost}} \times \mathbf{B} = \mathbf{u}_{\text{physical}} \times \mathbf{B}$). The idea of this approach is to set the plasma velocity at the surface $\mathbf{u}_{\text{surface}} = (\mathbf{u}_{\text{ghost}} + \mathbf{u}_{\text{physical}})/2$ to be perpendicular to the local magnetic field as described in detail in Zhou et al. (2019).

For the simulation outer boundaries, we specify the boundary conditions using idealized solar wind and IMF conditions at the upstream boundary ($X = 8 R_M$) and apply floating boundary conditions to all the other five boundaries of the rectangular simulation domain to allow the super-magnetosonic solar wind to leave the system freely. For all the simulations performed in this study, the upstream conditions (see Table 1) are fixed in time. Because we aim to investigate how Mercury's magnetopause reconnection depends on the upstream conditions, specifically the solar wind Alfvénic Mach number (M_A) and the IMF orientation, the simulations presented here

can be divided into two groups: one with $M_A = 6$, which may be considered nominal solar wind driving, and another with $M_A = 2$, which can be deemed as strong driving. Each Mach number group then consists of three simulations with the same IMF strength but different orientations characterized by the clock angle (i.e., the angle of the IMF vector in the YZ plane relative to the $+Z$ axis measured counter-clockwise when viewed from the Sun) resulting in three different shear angles between the IMF and Mercury's magnetospheric field at the low-latitude dayside magnetopause, that is, 90, 135 and 180°. As shown in Table 1, the solar wind density, velocity and temperature chosen for the simulations fall within the typical ranges observed at Mercury. The design of the solar wind input parameters enables us to make systematic comparisons between (a) simulations with the same IMF orientation but different Alfvénic Mach number and (b) simulations with the same Mach number but different IMF orientations, which will be described in detail in the following sections.

3. Simulation Analysis and Results

In this section, we present our simulation results for different upstream conditions listed in Table 1 focusing on the formation and properties of FTEs and their role in driving the global dynamics. Section 3.1 gives an overview of the typical structure and properties of the FTEs formed in our Hall-MHD simulations. Section 3.2 describes the quasi-automated algorithm we have developed to identify FTEs and extract their properties from the simulations. Section 3.3 shows the statistical results on the identified FTEs. In Section 3.4, we assess the contribution of FTEs to Mercury's Dungey cycle and how this contribution varies depending on the upstream conditions.

3.1. Spatial Structure and Temporal Evolution of Simulated FTEs

To illustrate the 3D structure of the FTEs seen in our simulations, we show in Figure 1 an example of FTE extracted from Run #2 (in Table 1), which corresponds to $M_A = 6$ and IMF clock angle of 135°. The magnetopause surface is extracted from the simulation based on the analytical magnetopause model first introduced in Shue et al. (1997). The colors on the surface indicate the normal component of the magnetic field (B_n) with respect to the modeled magnetopause surface (red colors indicate magnetic fields pointing away from the Mercury and blue colors indicate the opposite direction) and the black lines show magnetic field lines traced from locations within the FTE. Rope-like structure and resultant bipolar B_n signature of FTE can be seen clearly from Figure 1. In addition to providing global context for the example FTE in 3D, the Shue magnetopause model presented here is also used in our quasi-automated algorithm to identify FTEs whose detail will be discussed in the next section (Section 3.2).

Figure 2 shows a snapshot of B_y contours in $X-Z$ plane with magnetic field lines superimposed to delineate the magnetospheric configuration from another simulation, Run #1 ($M_A = 6$, IMF clock angle = 180°). The magenta ellipses outline the boundaries of two identified FTEs whose cross-section areas are fitted with 2D ellipses that are used for evaluating the amount of magnetic flux carried by FTEs (see detailed discussion later in the text). Both FTEs seen in this example not only have a loop-like magnetic geometry (as shown by the field lines) but also exhibit enhancements in the axial component of the magnetic field (as indicated by the colors), which is pointing in the $-Y$ direction in this case.

While Figures 1 and 2 provide single snapshots of the 2D and 3D structure of simulated FTEs, those FTEs, once formed in our simulations, all undergo substantial changes as they interact with the surrounding plasma and magnetic field. To illustrate how FTEs evolve in time, we show in Figures 3 and 4 a series of snapshots of B_y contours with sampled magnetic field lines in $X-Z$ plane in a similar format as in Figure 2. The results shown here were extracted from two simulations with Figure 3 from Run #1 where $M_A = 6$ and Figure 4 from Run #4 where $M_A = 2$. In both runs, the IMF clock angle is kept at 180°. The time separation between consecutive frames is 2 s. Mercury's conducting core is shown as black filled half-circle capped at $0.8 R_M$ and its surface is represented by the red half-circle at $r = 1 R_M$. FTEs in Figures 3 and 4 show up as concentric magnetic loops with a significant out-of-plane magnetic component (B_y). In the $M_A = 6$ case (Figure 3), initially at the start of the series ($T = 36$ s), there are five FTEs present over a large range of latitudes on the magnetopause: one each near the northern and southern cusp and another three at low latitudes. Following the labeled FTEs through the various snapshots shows that they typically go through a growth phase first in which their size and core field strength keep increasing, and then experience a decay phase in which they gradually dissipate while passing through the cusp region. During the time interval of ~ 15 s shown in Figure 3, four new FTEs are observed to

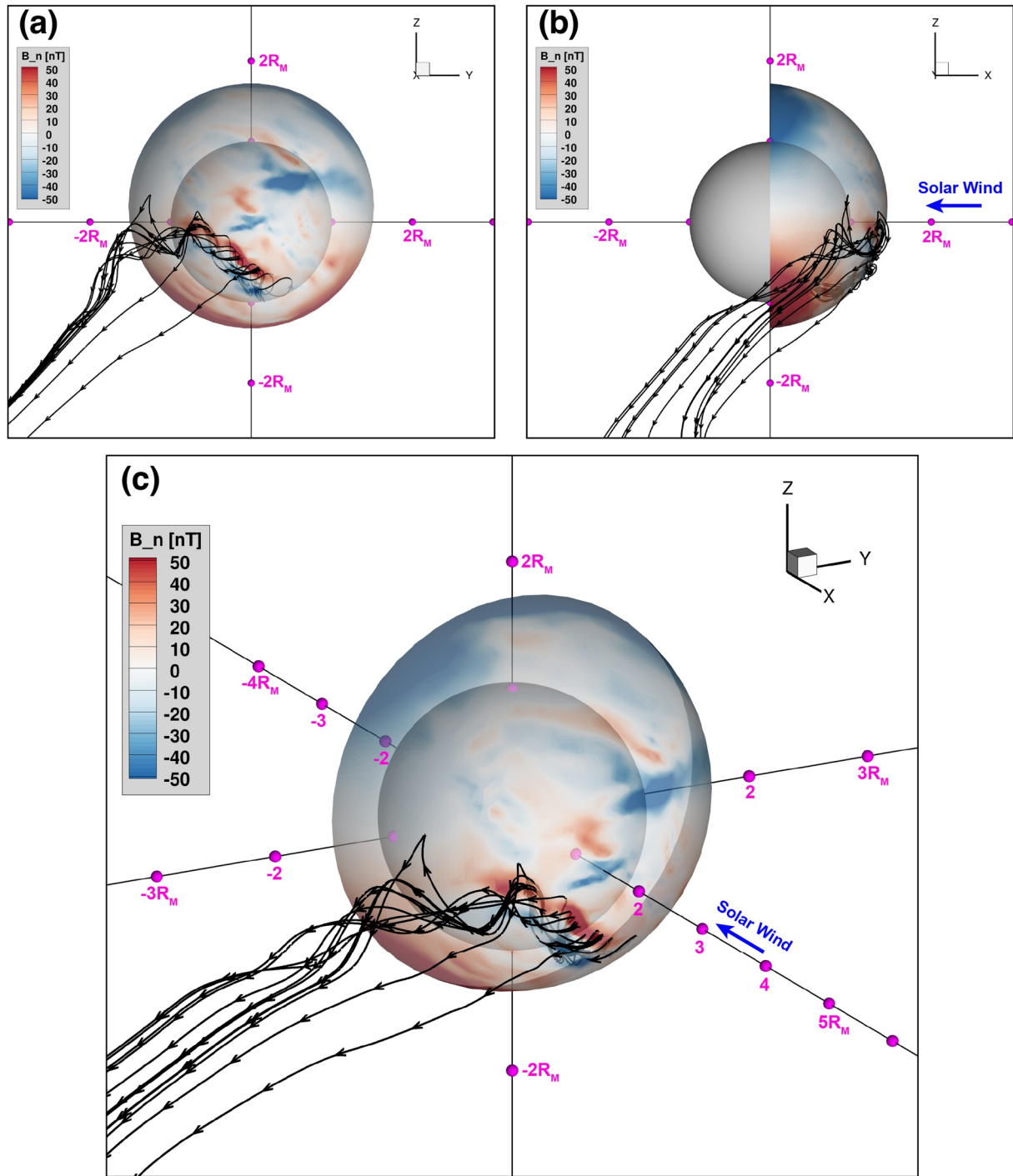


Figure 1. An flux transfer event (FTE) example from Run #2 corresponding to $M_A = 6$ and interplanetary magnetic field clock angle of 135° . The three panels show the FTE structure as viewed from different perspectives: (a) YZ plane as viewed from the solar wind; (b) XZ plane as viewed from the dawn side; (c) 3D view. In all three panels, color contours of B_n (the magnetic field component normal to the magnetopause) are shown on the magnetopause surface extracted from the simulation. Red colors indicate magnetic field pointing outward away from Mercury and blue colors indicate inward-pointing magnetic field. The black lines with arrows are sample field lines with one end connected to Mercury and the other end connected to the solar wind. Mercury is represented by a gray sphere with a radius of $1 R_M$ in the center. The FTE shown here is clearly characterized by rope-like magnetic topology and bipolar B_n signatures.

form and they essentially follow a similar evolution from growth to decay. For the $M_A = 2$ case (Figure 4), FTEs typically are found to have smaller size than that seen in the $M_A = 6$ case (Figure 3). The series of snapshots start with 3 FTEs initially ($T = 28$ s), but six additional FTEs are formed over the course of 15 s, suggesting a more frequent occurrence of FTEs compared to the $M_A = 6$ case in Figure 3. In both the $M_A = 6$ and $M_A = 2$ cases shown

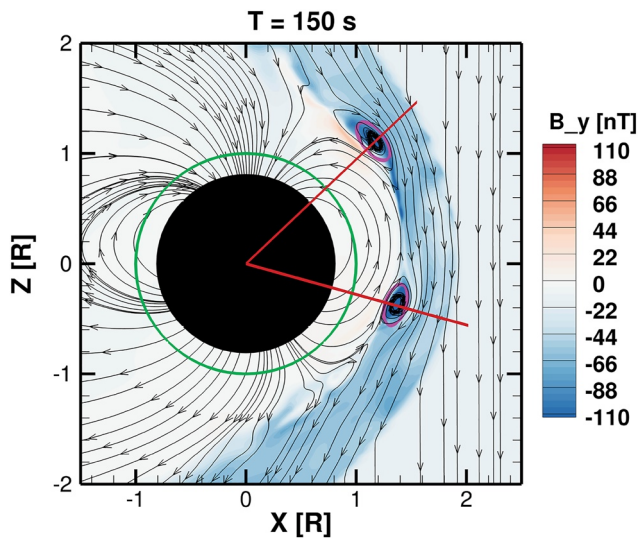


Figure 2. Snapshot of B_y contour in X - Z plane with magnetic field lines overlaid as black arrowed lines. The magenta ellipses outline the outer boundaries of two identified flux transfer events (FTEs), whose cross-sections are modeled as 2D ellipse in this study to quantify their magnetic flux. Two red straight lines going through the center of the FTE are used to measure FTE's size in the radial direction.

here for the IMF clock angle of 180° , most FTEs initially form close to the noon-midnight meridian (i.e., $LT = 12$ plane) and near the magnetic equator. Once formed, the FTEs propagate mostly along $\pm Z$ direction (either northward or southward). In contrast, as the IMF clock angle decreases (e.g., to 90° and 135°), the locations where most FTEs form in our simulation start to shift away from the noon-midnight meridional plane as well as in the north-south direction. This is because FTEs typically form near the primary reconnection X -line where the reconnection electric field peaks. As will be shown later in Section 4, the geometry of the reconnection X -line in our simulations exhibits a clear dependence on the IMF orientation, and as such the primary locations of where FTEs form are also dependent on the IMF orientation. Detailed statistics on various properties of the simulated FTEs will be presented and compared among different simulations in Section 3.3.

Another notable feature in Figures 3 and 4 is the common presence of multiple X -lines on the magnetopause surrounding FTEs, suggesting that multiple X -line reconnection is the underlying mechanism responsible for the formation of FTEs in our Hall-MHD simulations. To confirm this point, we have repeated Run #1 using an ideal MHD simulation model while keeping all the simulation setup and input parameters the same. We find that the magnetopause boundary in the ideal MHD simulation appears very quiescent with relatively steady reconnection arising from single X -line on the magnetopause. As a result, there are no FTEs formed in the ideal MHD simulation.

The behavior observed in the ideal MHD simulation is in sharp contrast with

the unsteady nature of reconnection and the presence of multiple X -lines on the magnetopause seen in the Hall MHD simulations.

The global model also allows us to extract plasma and magnetic field signatures associated with FTEs at fixed spatial locations, which makes it possible to compare directly with spacecraft measurements. As an example, Figure 5 shows the time series of key physical parameters, including plasma density, pressure and magnetic field vector components and magnitude, extracted from Run #1 at a virtual satellite located at $[X, Y, Z] = [1.26, 0, 0.93]R_M$ in MSO coordinates. The position of this satellite, being on the magnetopause north of the equator, gives us a clear view of the perturbations caused by FTEs as they pass by in the simulation. The red vertical intervals correspond to identified FTEs based on bipolar B_n signature, the detail of which will be discussed in the next section. One notable feature that immediately stands out in Figure 5 is that the typical duration of FTEs as seen by a virtual observer is quite short, on the order of a few seconds, which is consistent with MESSENGER observations of FTEs at Mercury (e.g., J. A. Slavin et al., 2012; W. J. Sun et al., 2020b). As will be shown later, the short duration of FTEs is a result of their small scale size and the relatively fast speeds at which they move along the magnetopause. Furthermore, FTEs are separated by a few to a couple of tens of seconds, indicating a quite frequent occurrence. Figure 6 is similar to Figure 5 but for results extracted from Run #4, which differs from Run #1 in the solar wind M_A used. Comparing Figure 5 with Figure 6, we find that for Run #4, which corresponds to a lower M_A condition, the spacing between neighboring FTEs is smaller, the typical duration of FTEs is shorter and consequently the number of identified FTEs is larger compared to Run #1. This comparison clearly shows that lower M_A solar wind and IMF conditions lead to a more dynamic dayside magnetopause and more frequent formation of FTEs, which is in general agreement with previous MESSENGER observations (e.g., W. J. Sun et al., 2020).

3.2. Automated Method for FTE Identification

Given the large number of FTEs formed in our simulations, we have developed an automated method to consistently identify FTEs in the simulations and extract the physical properties of FTEs (e.g., size, speed, magnetic flux content, etc.) that will be used later in our statistical analysis of the simulated FTEs. When the IMF has a significant southward component, because of the small size of Mercury's magnetosphere, almost all the FTEs formed in the simulation cut across the noon-midnight meridional plane (XZ plane). Such a behavior allows us to identify

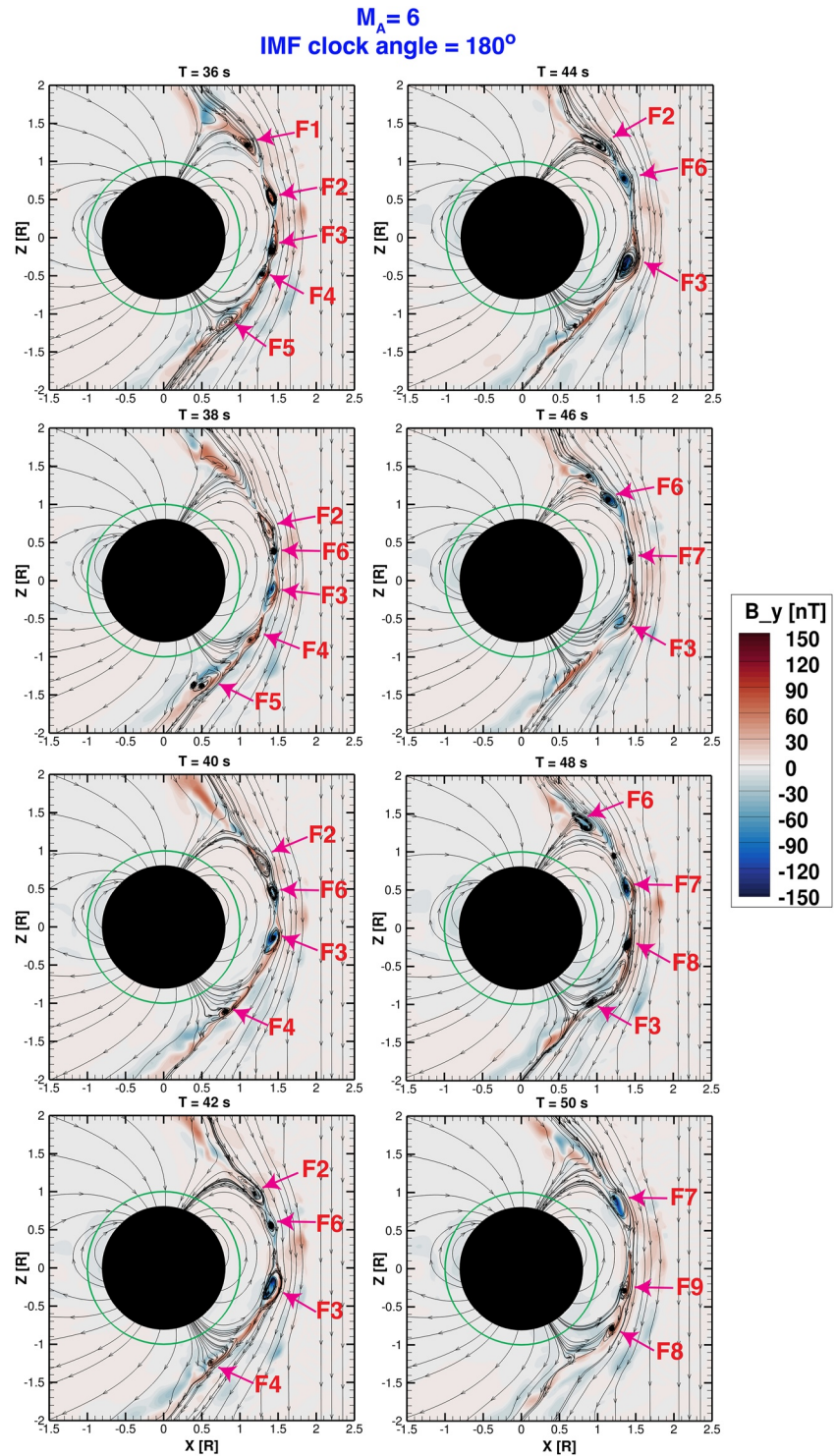


Figure 3. Multiple snapshots of B_y contours and sample magnetic field lines in the X - Z plane extracted from two simulations for comparison. The results are extracted from Run #1 ($M_A = 6$, interplanetary magnetic field clock angle = 180°) at a time cadence of 2 s. The green circle represents Mercury's surface at $r = 1 R_M$ and the black filled disk represents Mercury's core with an assumed radius of $0.8 R_M$. Labels and arrows are added to each panel to track individual flux transfer events.

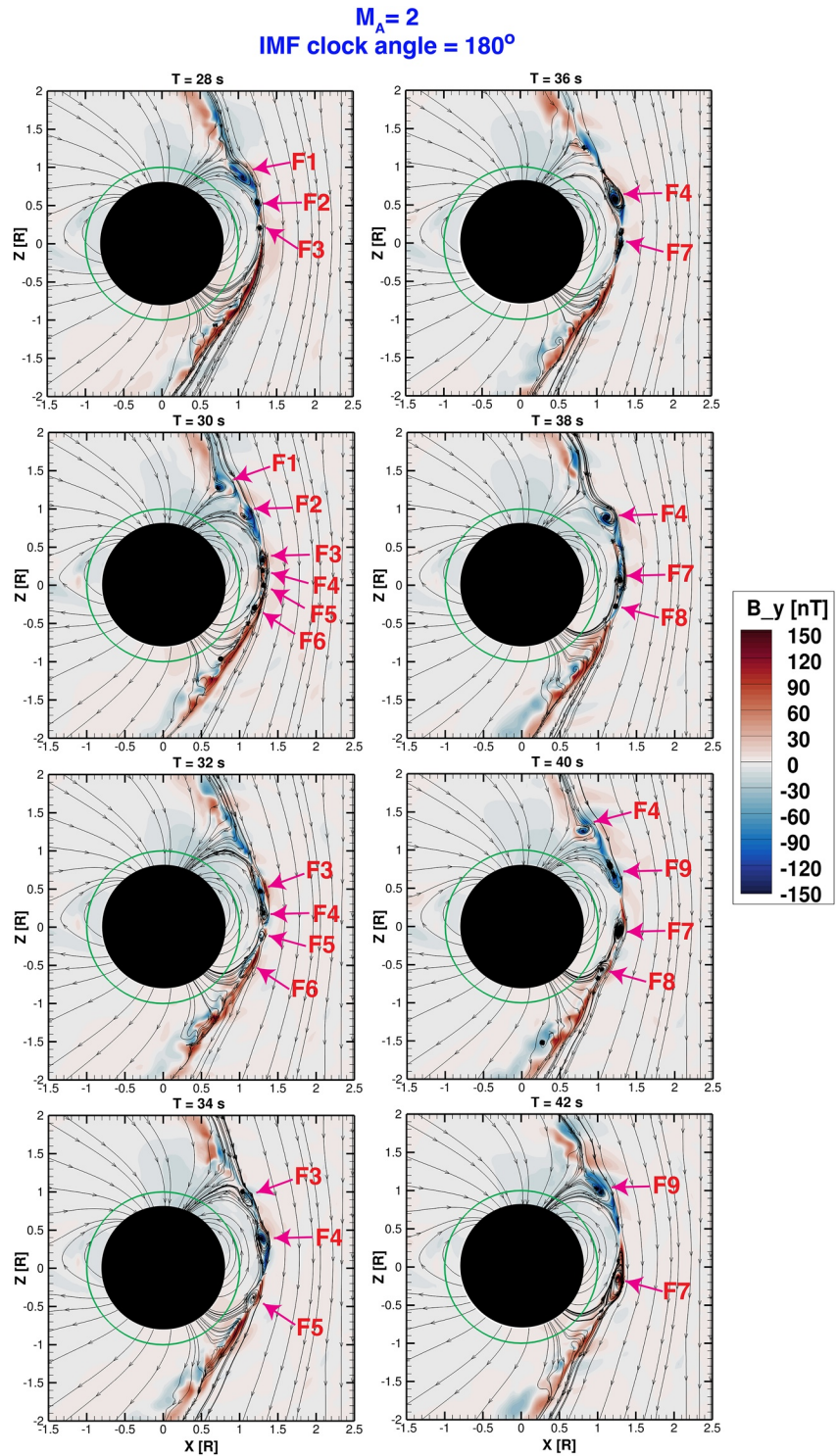


Figure 4. Same as Figure 3 but for Run #4 ($M_A = 2$, interplanetary magnetic field clock angle = 180°).

FTEs along the intersection of the magnetopause with the noon-midnight meridian for cases when the IMF has a significant southward component (or large shear angle). For small shear angle cases, magnetopause reconnection sites and resultant FTEs tend to occur away from the noon-midnight meridian, and for those cases we sample meridional planes at both morning and afternoon local times to capture FTEs, which will be explained later. In general, because of the rope-like structure of FTEs, the magnetic field component normal to the magnetopause

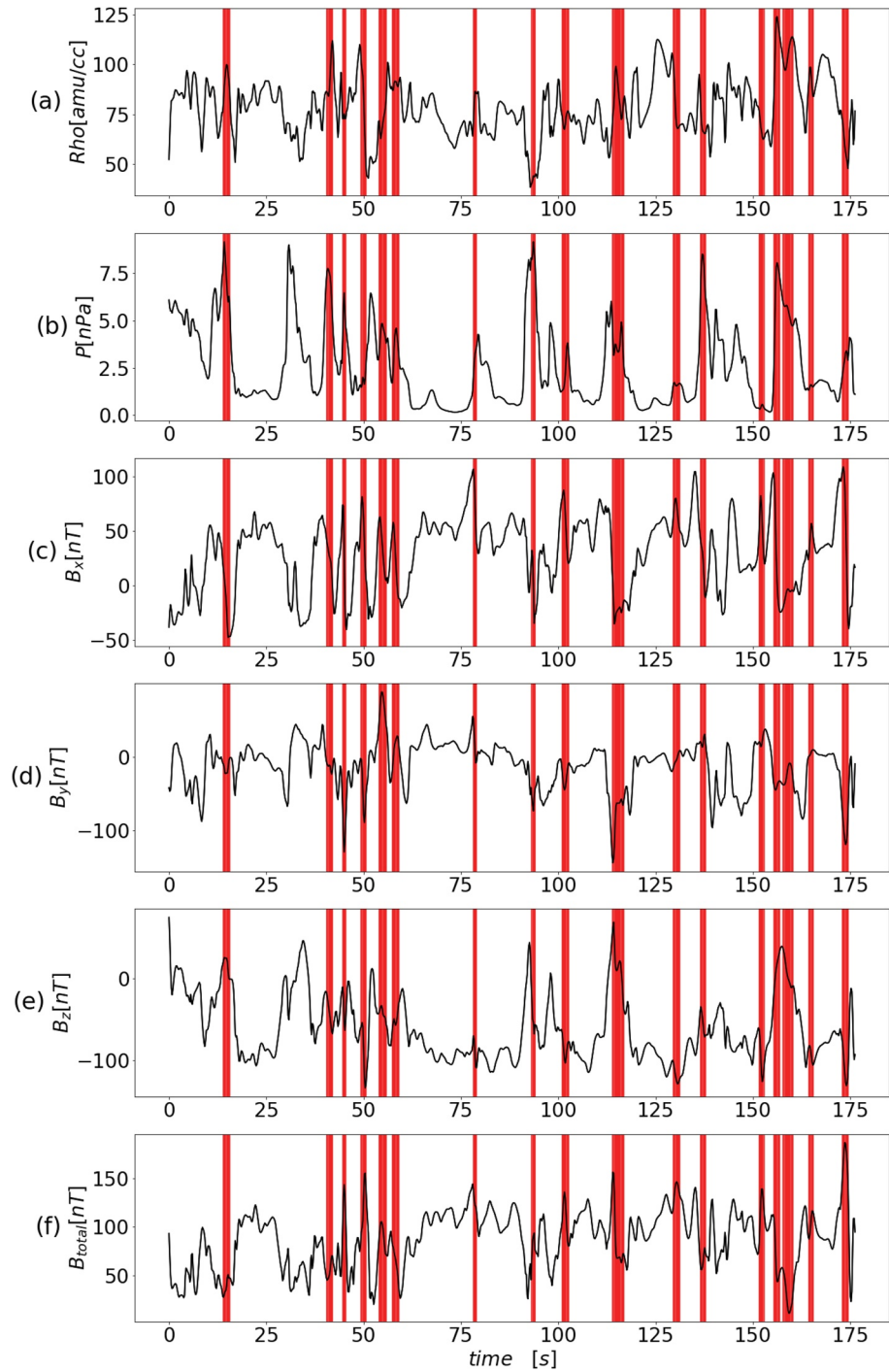


Figure 5. Time series of simulated physical parameters (a) plasma density, (b) plasma pressure, (c–e) B_x , B_y , B_z , and (f) magnetic field strength, observed by a virtual satellite located at $[X, Y, Z] = [1.26, 0, 0.93] R_M$ from Run #1 ($M_A = 6$, interplanetary magnetic field clock angle = 180°). The red vertical intervals correspond to identified flux transfer events based on bipolar B_n signature.

(B_n , where a positive value corresponds to magnetic field pointing toward the magnetosheath) is expected to have a bipolar pattern associated with each FTE, which means that pairs of positive-negative B_n on the magnetopause surface can be used as a selection criteria for identifying potential FTEs. Since Mercury's intrinsic magnetic field points from south to north near the equator, an FTE will always have positive B_n for the upper half of the magnetic loop and negative B_n for the lower half. The clear ordering of positive-negative B_n in the latitudinal

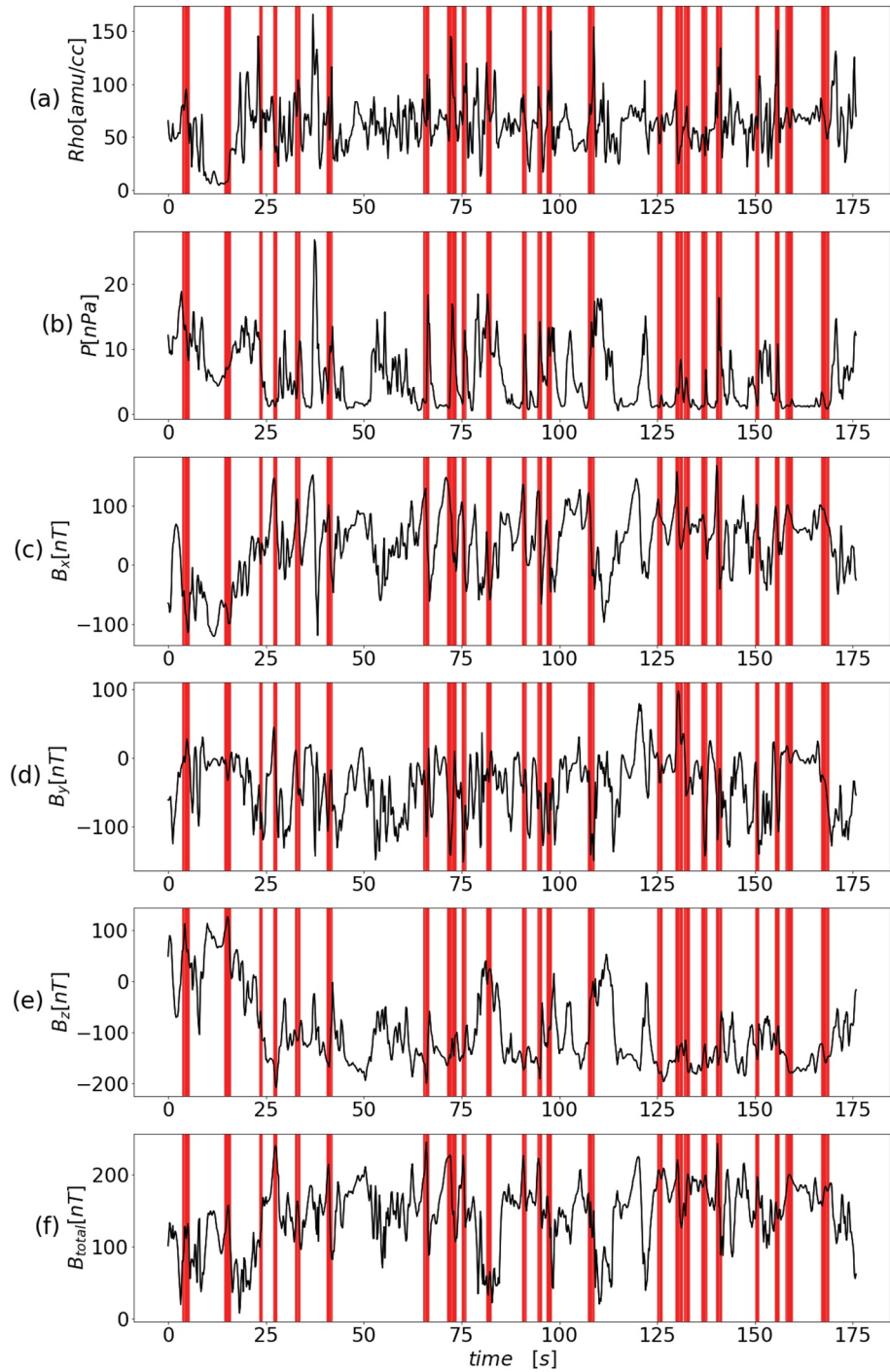


Figure 6. Same as Figure 5 but for results extracted from Run #4 ($M_A = 2$, interplanetary magnetic field clock angle = 180°) at a virtual satellite located at $[X, Y, Z] = [1.16, 0, 0.87] R_M$, which is also on the sheath side of the magnetopause boundary.

direction gives another criteria to identify FTEs in our automated algorithm. The existence of FTEs and its dynamic nature presents a challenge to determine the exact location and shape of the magnetopause boundary that separates the magnetosphere and magnetosheath. In a previous modeling study of Ganymede's magnetosphere, Zhou et al. (2020) used time-averaged $B_z = 0$ surface as an estimation for Ganymede's magnetopause. However, such an approach is less ideal for Mercury because (a) Mercury has a very dynamic magnetopause such that the actual magnetopause at a given timestep could deviate significantly from the time-averaged $B_z = 0$ surface, and (b) the presence of FTEs creates indentations/bulges on the $B_z = 0$ surface and the resultant irregular shape makes

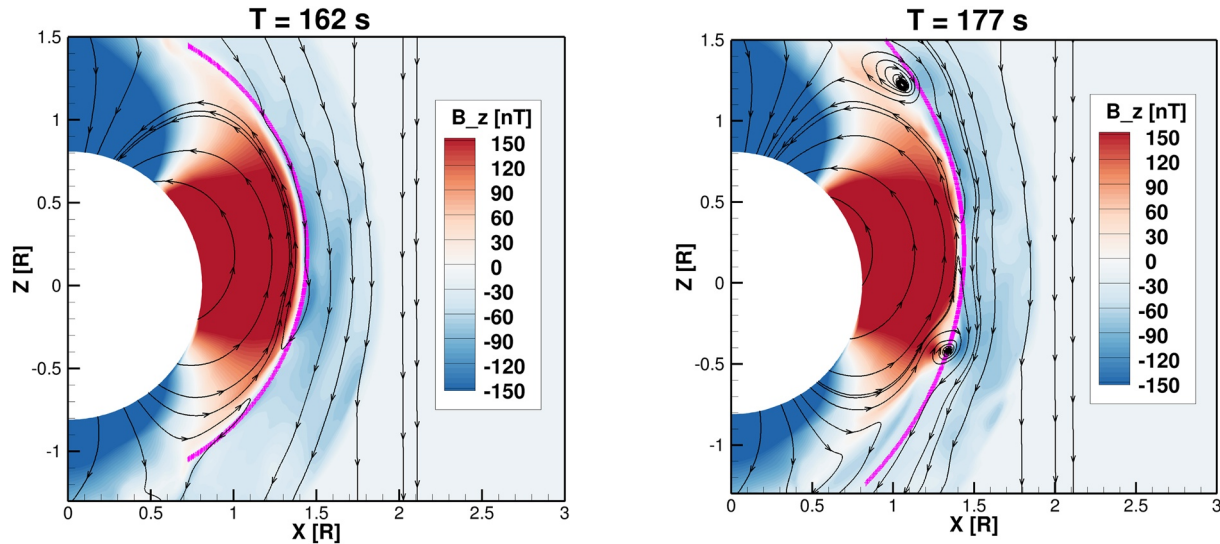


Figure 7. Demonstration of fitting the Shue et al. empirical model to the simulated magnetopause boundary. The two panels show results from two timesteps ($T = 162$ and 177 s) extracted from Run #2 ($M_A = 6$, interplanetary magnetic field clock angle = 135°) with sampled magnetic field lines in the X - Z plane. The background colors show B_z contours in the XZ plane and the magenta curve shows the fitted magnetopause model.

it difficult to identify FTEs based on bipolar B_n signatures. Considering these factors, in this study we employ the empirical magnetopause model by Shue et al. (1997) as an approximation to determine the normal component of magnetic field B_n on the magnetopause. By analyzing the MESSENGER observations of magnetopause crossings, Winslow et al. (2013) have shown that the Shue model works reasonably well for Mercury. The analytical form of the Shue model is given as:

$$r = r_0 \left(\frac{2}{1 + \cos \theta} \right)^\alpha, \quad (8)$$

where r is the radial distance from the center of the planet's dipole and θ is the angle between the radial direction and the $+X$ direction in MSO coordinates. Both r_0 and α are free parameters used to determine the shape of the empirical magnetopause. Specifically, r_0 is the subsolar magnetopause standoff distance and α is a parameter that decides the level of tail flaring. We adjust r_0 and α to match the Shue magnetopause model with the simulated magnetopause for every timestep on which the simulation results were saved such that the constantly changing shape and motion of the magnetopause are accounted for. The approach we used to determine r_0 and α for every timestep is as follows: (a) Launch multiple horizontal lines ($Z = \text{constants}$) in the meridional plane of interest, and then identify the magnetopause boundary locations as the points where large plasma density jumps are observed, (b) Use the $Z = 0.2$ horizontal line (corresponding to the magnetic equator) to determine the magnetopause subsolar standoff distance r_0 . Take r_0 determined from the previous step to calculate α using Equation 8 for the other horizontal lines at different Z distances and then take the average value to be α for this particular timestep. As a demonstration, Figure 7 shows the result of our dynamically fitted Shue model (magenta line) for Run #2 in the XZ at $Y = 0$ plane for two different timesteps. Sampled magnetic field lines are shown as black stream traces in Figure 7 to illustrate the topology of dayside magnetic field. The background colors in Figure 7 represent contours of B_z , where the $B_z = 0$ contour (white color) provides a crude indication of where the magnetopause is. As can be seen, by dynamically adjusting the values of r_0 and α in the Shue empirical model we are able to obtain reasonably good fits to the simulated magnetopause as it varies with time. This dynamic fitting approach, compared to time-averaged $B_z = 0$ surface, not only addresses the unsteady nature of Mercury's magnetopause but also yields a relatively smooth transition of the magnetopause normal direction between different timeframes.

By applying the magnetopause fitting procedure to the simulation output we can then extract physical parameters of interest along the magnetopause boundary from different timesteps and then examine the time evolution of the extracted parameters to identify FTEs and determine their physical properties, such as spatial size, speed of motion and the amount of magnetic flux contained. A useful way to visualize the extracted simulation results is to construct a time-latitude (t - θ) map as shown in Figure 8, which corresponds to Run #2 ($M_A = 6$, IMF clock angle = 135°). The extracted parameters shown as color contours in this particular example are (a)

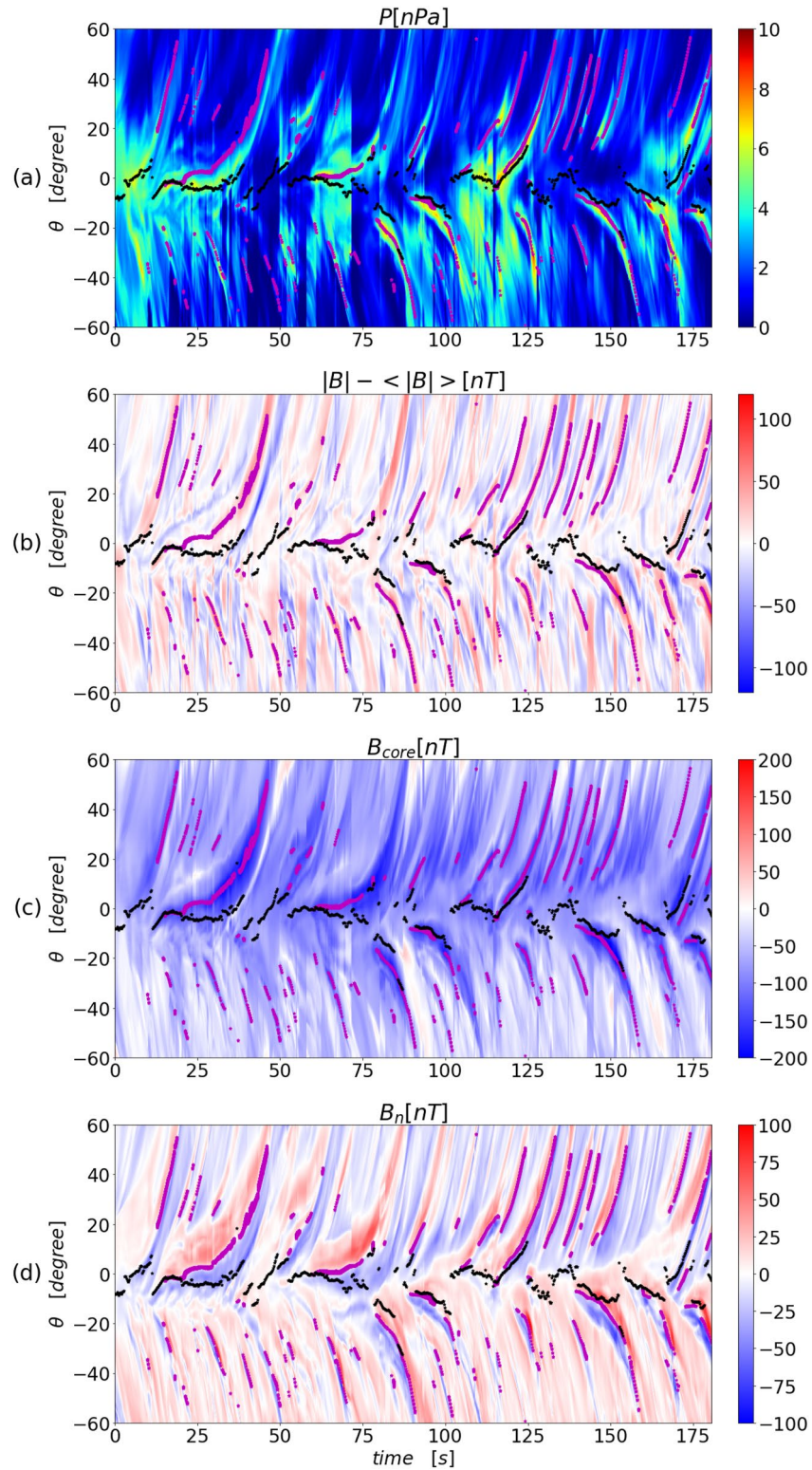


Figure 8. Time-latitude map to characterize the temporal variation of physical parameters along the magnetopause in the noon-midnight meridian (LT = 12) for Run #2 ($M_A = 6$, interplanetary magnetic field clock angle = 135°). The extracted physical parameters shown here as the background colors are: (a) Plasma pressure P , (b) Perturbations to the magnetic field strength, (c) flux transfer event (FTE) core field, B_c , and (d) Magnetic field component normal to the magnetopause, B_n . The magenta dots superimposed on each panel represent the centers of those identified FTEs and the black dots mark the flow diverging points near the magnetopause. The X-axis shows the simulation time in seconds and the Y-axis represents the magnetic latitude in degrees.

plasma pressure (P), (b) perturbations to the magnetic field strength, (c) FTE core field (B_c), and (d) the normal component of the magnetic field (B_n). Note that for panel (b), the perturbation to the magnetic field magnitude is measured with respect to the average value of $|B|$ in a 5-s sliding window. The method we use to calculate the core field (B_c) shown in panel (c) will be described in detail in Section 3.3.

Figure 9 is similar to Figure 8 but for Run #3 ($M_A = 6$, IMF clock angle = 90°). For this IMF configuration, most FTEs do not form near the noon-midnight meridian, but instead they are produced primarily in the northern-dawn and southern-duck quadrants of the magnetopause. Once the FTEs have formed, their subsequent motion tends to follow the direction of the reconnection outflow, which is generally perpendicular to the X -line. As such, the FTEs formed under this IMF configuration propagate mostly in a direction that deviates from the $\pm Z$ -direction and has a significant Y -component (almost along the diagonal direction in the YZ -plane). Therefore, instead of using the $LT = 12$ meridian as described above for larger IMF clock angle cases, for simulations with 90° IMF clock angle (Runs #3 and #6) we identify FTEs in two meridional planes corresponding to $LT = 09$ and $LT = 15$, and then add the results together to obtain the total number of unique FTEs. Figure 9 shows the results from the $LT = 15$ cut for Run #3. We have verified that no FTE in our simulation extends in the azimuthal direction to intersect with both the $LT = 09$ and 15 cut planes, which ensures that no FTE is counted twice in our statistics.

As explained above, potential FTEs would show up in the time-latitude map as pairs of positive-negative B_n (red and blue stripes in Figures 8d and 9d). Based on this expected B_n signature associated with FTEs, we have developed an automated identification method consisting of the following steps: (a) Identify the points between red and blue stripes that correspond to $B_n = 0$, (b) Measure the minimum and maximum values of B_n along the vertical (latitudinal) direction, (c) Apply a 20 nT threshold on the absolute values of B_n extrema to filter out ineligible red-blue stripes, (d) Visually check the 3D magnetic topology of all candidate FTEs and remove those that do not exhibit a rope-like structure. The 20 nT threshold applied in our identification algorithm was inspired by a previous study of Earth's FTEs (T. R. Sun et al., 2019), which used 5–10 nT as the threshold. However, in Mercury's case we have found that using 5 or 10 nT yields many false positive detections. For example, when using 10 nT as the criterion in our automated method we found that about 40% of those identified FTEs with desired positive-negative B_n pairs are false positives for Run #1 after manually checking their 3D magnetic field lines. This is likely due to the fact that intense reconnection occurring at Mercury's magnetopause causes large, local variations in the magnetopause shape in the simulation that results in significant B_n fluctuations. We have tested different thresholds of B_n and determined that 20 nT works reasonably well for our analysis in that the set of selection criteria combined are robust to capture the vast majority of FTEs in our simulations and at the same time conservative enough to filter out most of the false positives.

We have applied the automated algorithm to the output from all six simulations at 0.2 s cadence to identify FTEs. Note that the total duration of the model output that enters our analysis varies case by case ranging from ~ 150 to 200 s, which is comparable to the typical timescale of Mercury's Dungey cycle. The total number of unique FTEs identified is tabulated in Table 2 for all six simulations. One apparent trend that can be noticed in Table 2 is that the number of FTEs formed in the simulation increases with decreasing solar wind M_A and increasing IMF clock angle, which is consistent with the findings from the recent MESSENGER survey of FTE showers at Mercury (W. J. Sun et al., 2020b). Detailed statistics of simulated FTE properties and comparisons with observations will be presented in Section 3.3.

To follow the time evolution of FTEs that will feed into our statistical analysis later on, we also need to determine the centers of the FTEs, which can be readily identified in the B_n time-latitude map (e.g., Figures 8d and 9d) as $B_n = 0$ points (magenta dots). Tracking the centers of FTEs in time allows us to directly estimate their speed of motion as well as other properties of FTEs, which will be presented in the next section. By overplotting the FTE centers onto the other panels of Figures 8 and 9, we can cross-compare different physical parameters that provide useful insight into the structure of FTEs. For instance, panels (a–c) in Figures 8 and 9 indicate that most FTEs seen in our simulations show enhancements in plasma pressure, core field and total magnetic field strength near the FTE center, which are typical characteristics of FTEs observed at Mercury (e.g., J. A. Slavin et al., 2012; W. J. Sun et al., 2020b). Another interesting feature in Figures 8b and 9b is that most FTEs have trailing regions where the magnetic field is depressed compared to the background. Similar modeling results have been reported previously by Kuznetsova et al. (2009) who found magnetic field cavities in the wake of FTEs from their high-resolution simulations of Earth's FTEs.

The black dots in Figures 8 and 9 represent the locations on the magnetopause where the plasma flow speed reaches its minimum value. As a good approximation, those black dots can be deemed as flow diverging points that separate northward and southward moving plasma flows on the magnetopause. In the examples shown here

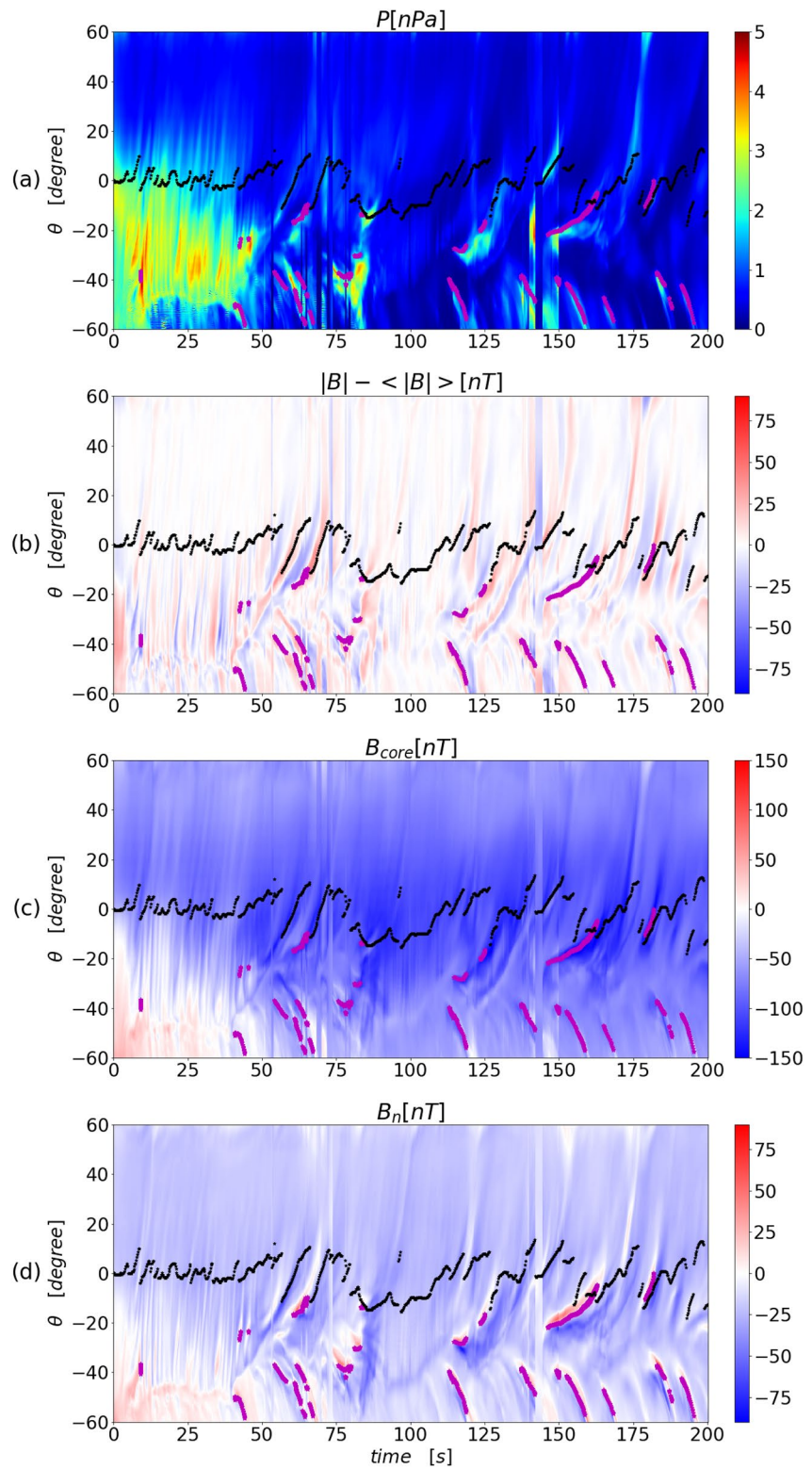


Figure 9. Same as Figure 8, but for Run #3 ($M_A = 6$, interplanetary magnetic field clock angle = 90°). The results shown here are extracted from the LT = 15 meridian on the dusk side.

Table 2
Total Number of Unique Flux Transfer Events (FTEs) and Average Occurrence Rate for Different Simulations

		Interplanetary magnetic field (IMF) clock angle					
		180°		135°		90°	
Solar wind Alfvénic Mach number	$M_A = 6$	Total No.: 52	Occur. Rate: 1 FTE every 3.4 s	Total No.: 42	Occur. Rate: 1 FTE every 4.2 s	LT = 09: 8 LT = 15: 15 Total No.: 23	Occur. Rate: 1 FTE every 8.7 s
	$M_A = 2$	Total No.: 68	Occur. Rate: 1 FTE every 2.6 s	Total No.: 60	Occur. Rate: 1 FTE every 2.7 s	LT = 09: 33 LT = 15: 16 Total No.: 49	Occur. Rate: 1 FTE every 3.2 s

Note. For the 90° IMF clock angle cases we have identified FTEs in two meridional planes (LT = 09 and 15), so the corresponding column gives the number of FTEs in different planes and the total count.

for two different IMF orientations, we find that the flow diverging point in the simulation is, in general, located very close to Mercury's magnetic equator with some fluctuations caused by reconnection outflows, which is consistent with the general expectation that the large-scale structure of the solar wind-magnetosphere interaction is controlled primarily by symmetries associated with the planetary internal field. In Figure 8, which corresponds to IMF clock angle of 135°, the northward and southward moving FTEs are generally well divided by a separatrix close to the magnetic equator and hence the flow diversion region, consistent with the geometry of the primary X-line expected for this particular IMF orientation (see Figure 13 and associated discussions in Section 5). In contrast, in Figure 9 that corresponds to 90° IMF clock angle case, the separatrix between northward and southward moving FTEs is shifted to the south (~30° southern latitude) in the dusk meridian and shifted to the north in the dawn meridian (not shown). Again, such a behavior can be readily understood in terms of the geometry of the primary X-line expected for an IMF configuration with a dominant y-component (see Figure 13 and associated discussions in Section 5). Because the flow diversion region is still located near the magnetic equator, FTE formation and their subsequent motion are restricted almost exclusively to the south of the flow diverging points on the dusk side. A similar pattern is seen on the dawn side but with most FTEs seen north of the flow diversion region. These simulation results suggest it is important to take into account both the reconnection geometry and large-scale plasma flows, especially the magnetosheath flow, in considering FTE formation and propagation.

3.3. Statistical Survey of Simulated FTEs

Here we present a statistical analysis on the simulated FTEs identified by our automated method. The primary properties of FTEs we focus on in this work are their occurrence rate, spatial size, traveling speed, core field strength and magnetic flux content.

The FTE occurrence rate can be readily obtained based on the total number of FTEs identified within the duration of the simulation output, which is given in Table 2. For the external conditions considered in our work, FTEs are formed in the simulation every few seconds, with occurrence rates ranging from 2 to 9 s. Comparing the occurrence rates across different runs reveals a clear trend that FTEs are formed more frequently in the simulation with smaller solar wind Alfvénic Mach number, which leads to lower plasma beta in the magnetosheath, and larger IMF clock angle, which corresponds to stronger magnetic shear across the magnetopause boundary. Both the FTE occurrence rate and its dependence on the solar wind M_A and IMF orientation found in our Hall-MHD simulations are in good agreement with the results reported in a recent MESSENGER survey of FTE shower events at Mercury (W. J. Sun et al., 2020b).

The statistical results of other FTE properties, including size, traveling speed, core field strength and magnetic flux content, are shown as histograms in Figures 10–12. To facilitate comparison, we have paired the results from simulations with the same IMF clock angle but different solar wind M_A into one figure, that is, Figure 10 for 180° clock angle, Figure 11 for 135° and Figure 12 for 90°. Determining those FTE properties shown in Figures 10–12 from the simulation requires further analysis beyond the automated identification method described in Section 3.2, which we explain in the following.

First, we measure the size of an FTE as its characteristic scale length in the latitudinal direction along the magnetopause surface. Because of the loop-like structure of FTE's cross-section, the magnetic field normal component, B_n , normally would exhibit a bi-polar variation along the latitudinal direction. For a given timestep, we first find the

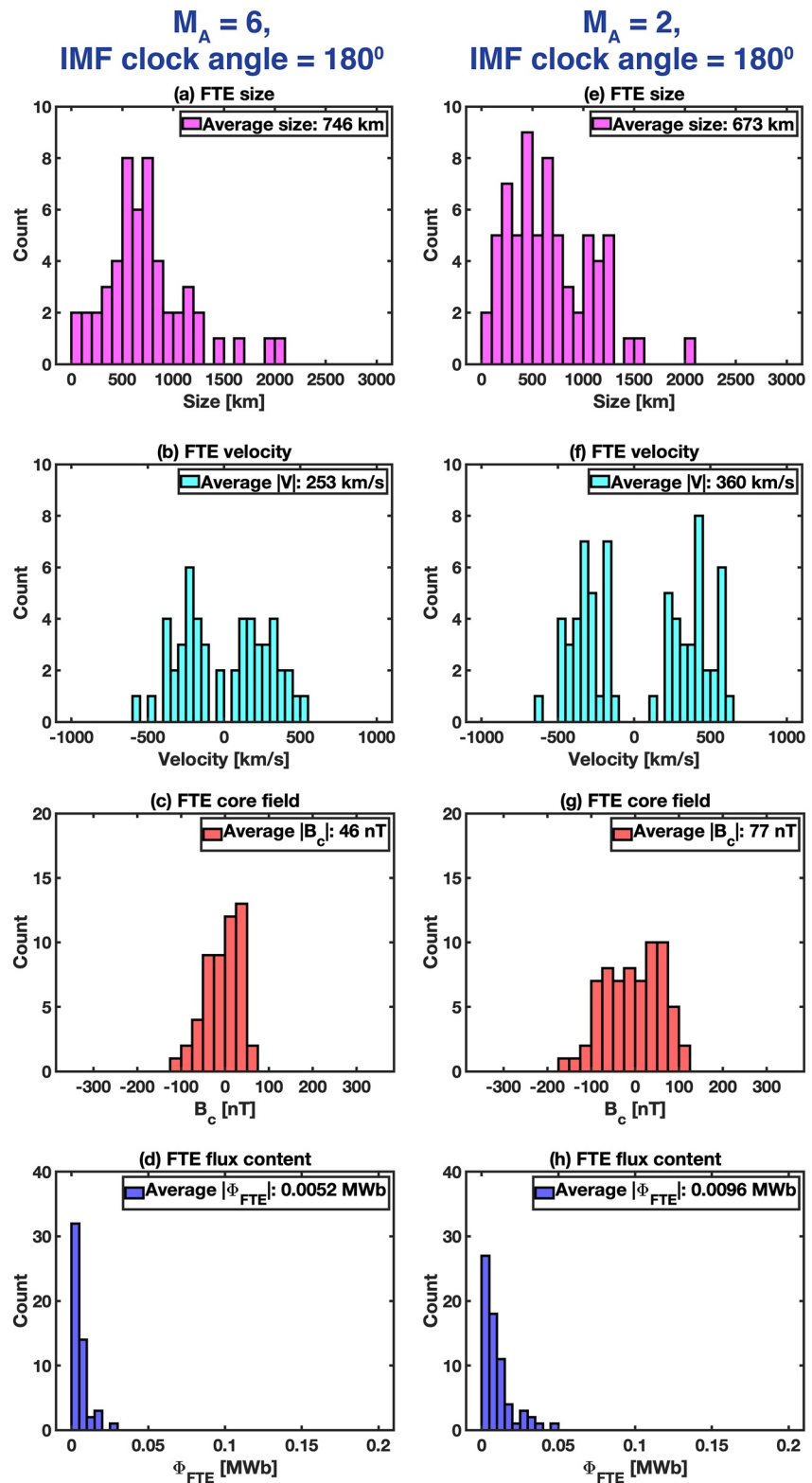


Figure 10. Histograms of various flux transfer event (FTE) properties for 180° interplanetary magnetic field (IMF) clock angle cases. (a and e) Average FTE size. (b and f) Average FTE velocity in the latitudinal direction. (c and g) Core field strength. (d and h) Magnetic flux carried by FTE. The left column corresponds to $M_A = 6$ and the right column is for $M_A = 2$.

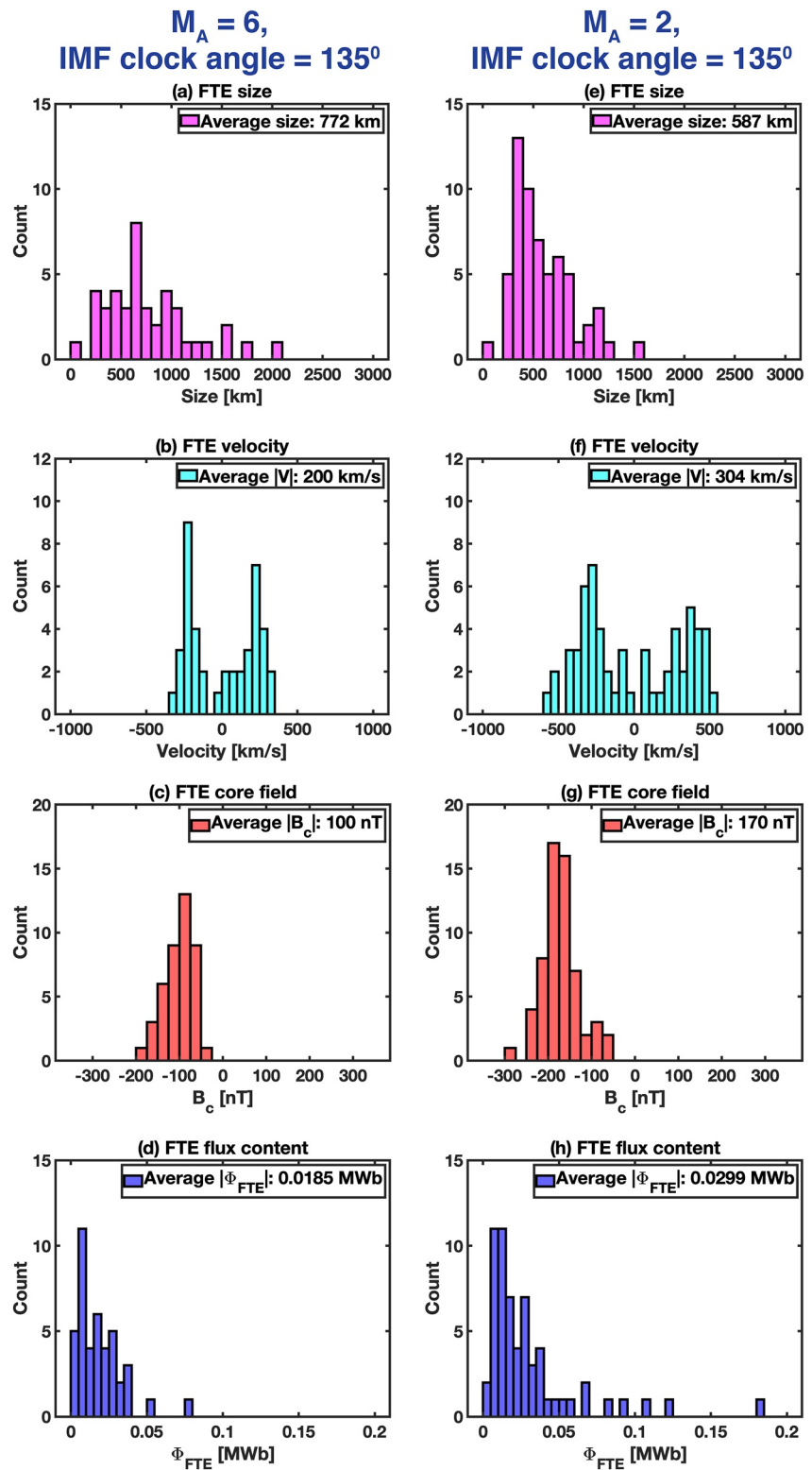


Figure 11. Same as Figure 10, but for 135° interplanetary magnetic field (IMF) clock angle cases.

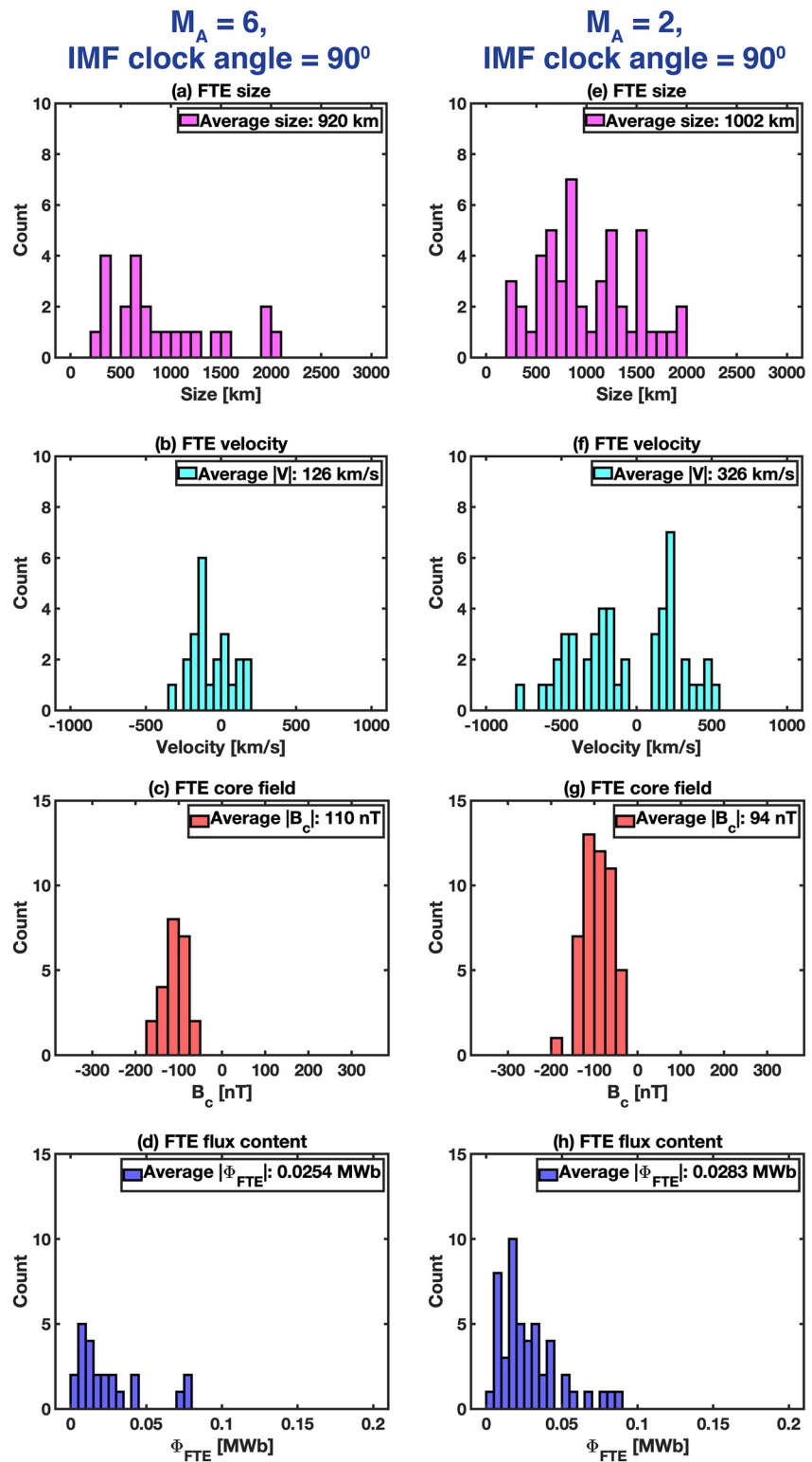


Figure 12. Same as Figure 10, but for 90° interplanetary magnetic field (IMF) clock angle cases.

maximum (positive) and minimum (negative) values of B_n associated with a particular FTE. The northern and southern outer boundaries of the FTE are then defined as the locations where B_n has decayed by $1/e$ (one e-folding distance) from its maximum and minimum values. The distance between the northern and southern boundary points approximately represents the length along the semi-major axis of the FTE's cross-section in the particular LT cut in which we identify the FTE. However, the FTE size we aim to quantify should be measured in the cross-section orthogonal to the axis of the FTE, whose orientation varies depending on the IMF clock angle. For example, for 180° IMF clock angle cases, the axes of FTEs formed in the simulations are approximately aligned with the Y -axis. However, when the IMF clock angle is smaller than 180° , the axes of FTEs are slanted with respect to the equatorial plane (see the example shown in Figure 1) at an angle that can be readily related to the IMF clock angle. To correct for this geometric effect, we define the FTE size to be the length measured in the LT multiplied with a factor $\cos(\theta_{\text{FTE}})$, where θ_{FTE} is the angle between the normal direction of the LT cut used to identify FTEs and the FTE axis. The value of θ_{FTE} is taken empirically as $0, 22.5, 45^\circ$ when the IMF clock angle is $180, 135, 90^\circ$, respectively. Moreover, since the size of an FTE changes in time as it interacts with the surrounding plasma and field, for each identified FTE we repeat the above procedure for every timestep (0.2 s cadence), and then average over 5 timesteps evenly sampled through its entire evolution to obtain the mean FTE size, which enters our statistical analysis. Panels (a) and (e) in Figures 10–12 show the distributions of average FTE size for simulations using different solar wind M_A . There is a wide spread in the size distribution for all simulations, with average FTE sizes ranging from <100 to ~ 2000 km. Comparing the results (shown in the legends of panels (a) and (e)) seen in different simulations reveals that the average FTE size is comparable between 180 and 135° IMF clock angle cases and becomes significantly larger in 90° IMF clock angle simulations. When the IMF clock angle is 180 or 135° , there is a higher percentage of small-size FTEs in $M_A = 2$ than in $M_A = 6$, and as a result, the average FTE size decreases with decreasing M_A . However, the 90° clock angle simulations do not appear to follow the same trend and the average FTE size increases with decreasing M_A .

The traveling speed of an FTE along the magnetopause can be determined from the aforementioned time-latitude maps (e.g., Figures 8 and 9) by tracking the slope of the curve connecting the identified FTE centers (magenta dots). Note that positive and negative slopes correspond to northward and southward motion, respectively, which are reflected in the sign of FTE traveling velocity shown in our statistics. It is evident from the examples shown in Figures 8 and 9 that the slope is not a constant for most FTEs, suggesting that FTEs commonly travel at varying speeds as they evolve in time, just like the size of FTEs discussed above. To account for this feature in our statistics, we calculate an average velocity for each FTE by taking the mean value of the estimated velocities from 5 timesteps evenly sampled through its lifetime. In estimating the FTE traveling velocity using the time-latitude maps, we have also taken into account the aforementioned geometric effect arising from projecting slanted FTEs onto LT cut planes by multiplying the speed extracted from a given LT plane with the same “ $\cos(\theta_{\text{FTE}})$ ” as used in calculating the FTE size. The distributions of average FTE traveling velocities are shown in panels (b) and (f) of Figures 10–12. For all six simulations, both northward (positive velocities) and southward (negative velocities) moving FTEs are present and the respective total numbers are roughly equal, consistent with the expectation based on the result discussed in Section 3.2 that symmetries in the planetary internal field predominantly control the global structure of the magnetospheric interaction and associated large-scale plasma flows. Overall the average FTE traveling speeds seen in the various simulations have a wide distribution ranging between a few tens of km/s to a few hundred km/s with peak distributions around 200 – 400 km/s, which are comparable to the typical value of 300 km/s assumed for FTE traveling speed in previous MESSENGER investigations of FTEs (e.g., Imber et al., 2014; W. J. Sun et al., 2020b). There is also the tendency that for the same IMF clock angle the distribution becomes wider for $M_A = 2$ cases compared to $M_A = 6$, indicating a more dynamic magnetopause under lower M_A solar wind conditions. By averaging over all FTEs seen in a given simulation, which is shown in the legends of panels (b) and (f), we find a consistent trend across all three pairs of simulations using the same IMF clock angle that the average FTE traveling speed increases with decreasing solar wind M_A . This result is consistent with theoretical expectation considering that FTE's traveling speed along the magnetopause largely depends on the flow speed in the reconnection outflow region, which scales directly with the Alfvén speed in the reconnection inflow region. Solar wind with lower M_A tends to result in higher Alfvén speed in the magnetosheath, thereby leading to faster reconnection outflows. When comparing the FTE speeds for simulations with the same M_A but different IMF clock angles, we find that the speed in general decreases with decreasing clock angle, with the exception from the case of $M_A = 2$ and clock angle = 90° (Figure 12f) where the average speed lies somewhere between the 135 and 180° cases. The general trend can be well understood in terms of how reconnection outflow speed depends on the reconnection magnetic field components on the two sides of the magnetopause (e.g., P. A. Cassak & Shay, 2007), which generally become weaker for smaller IMF clock angle with the same field magnitude.

The core field strength and magnetic flux content of FTEs are obtained through additional modeling of the structure of individual FTEs. In order to determine the total flux content carried by an FTE, we need to first identify its cross-section, which requires knowledge of the outer boundary of the FTE. While the latitudinal extent of an FTE can be determined using the method described above in the discussion of FTE size, the radial extent of an FTE can be estimated using a similar method. We first measure the maximum plasma pressure (P_{\max}) along the ray path going radially through the FTE's center (see the red lines in Figure 2), and then identify the inward and outward boundary locations of the FTE in the radial direction as the points along the radial ray where the plasma pressure has fallen off by $1/e$. Note that here we have used the plasma pressure, instead of B_n , as a criterion to search for the boundary locations in the radial direction mainly because B_n almost always vanishes along the radial ray passing through an FTE's center. Knowing the four boundary points of a given FTE in the latitude and radial directions, we then fit the FTE's cross-section as an ellipse (see the magenta ellipses in Figure 2), whose semi-minor axis and semi-major axis are equal to one half of the lengths in the radial and latitudinal directions, respectively. The total amount of magnetic flux carried by an FTE can then be obtained by integrating the out-of-plane magnetic field component (B_{out}) over the area of the ellipse representing the FTE's cross-section. The core field of an FTE (B_c) can also be estimated directly from the out-of-plane magnetic field component (B_{out}). Similar to the consideration in calculating the FTE size, we also take into account the geometric effect in our estimation of the FTE core field, which is defined as $B_c = B_{\text{out}} / \cos(\theta_{\text{FTE}})$, where B_{out} is the magnetic field component perpendicular to the LT cut used to identify FTEs and θ_{FTE} is the angle between the normal direction of the LT cut and the FTE axis. The value of θ_{FTE} is chosen to be 0, 22.5, 45° for IMF clock angles of 180, 135, 90°, respectively. Since the core field strength is non-uniform within the cross-section of an FTE and typically peaks near the center, we use the maximum core field in our statistics.

Similar to what is done for the other FTE parameters, we also take averages of the calculated magnetic flux content and core field over 5 evenly sampled timesteps through its lifetime for every identified FTE, whose distributions are shown in panels (c, g) and (d, h) of Figures 10–12. For the 180° IMF clock angle cases, FTEs' core fields can have either positive or negative polarity with respect to the dawn-dusk direction. In contrast, when the IMF has a significant B_y component, such as in the 90 and 135° clock angle simulations, the core fields associated with the vast majority of FTEs show the same polarity as that of the IMF B_y . This result is consistent with previous observations of FTEs at Earth. For instance, Kieokaew et al. (2021), found a similar trend in the FTEs observed by the Magnetospheric Multi-Scale mission and suggested that the polarity of FTE's core field is controlled mainly by the orientation of the guide field (e.g., IMF B_y) in the context of multiple X-line reconnection. The average core field strength ranges from ~50 to 170 nT in the six simulations, which is entirely consistent with that observed by MESSENGER during FTE shower events (W. Sun et al., 2022). For 180 and 135° clock angle simulations, the average core field strength shows significant increases (~70%) as the solar wind M_A decreases from 6 to 2. The 90° simulations show a somewhat different trend in that the average core field strength exhibits a modest decrease of ~15% between $M_A = 6$ and $M_A = 2$ cases.

As shown in panels (d) and (h), the average magnetic flux carried by individual FTEs ranges between 0.005 and 0.03 MWb, which is consistent with the range of values estimated by W. J. Sun et al. (2020) for the FTE shower events observed by MESSENGER. Furthermore, the upper end of the simulated FTE flux content of 0.03 MWb, which is a rare occurrence in the simulation, is comparable to the mean flux content (0.06 MWb) estimated for single “large” FTEs encountered by MESSENGER (Imber et al., 2014; J. A. Slavin et al., 2010). Comparing the simulation results for different IMF clock angle cases shows that under purely southward IMF conditions (180° cases), FTEs tend to carry less flux compared to the cases when the IMF contains a large B_y (135 and 90° cases). Furthermore, the average FTE flux content is comparable between the 135 and 90° clock angle cases, which is in general agreement with the result of very weak dependence on IMF clock angle identified in the W. J. Sun et al. (2020) MESSENGER survey. For the same IMF clock angle, individual FTEs on average carry a larger amount of open flux under lower solar wind M_A conditions, which is, again, in agreement with the trend found in the W. J. Sun et al. (2020) MESSENGER study.

3.4. FTE Contributions to Global Dynamics

Previous studies based on MESSENGER observations (e.g., J. A. Slavin et al., 2012; Imber et al., 2014; W. J. Sun et al., 2020b) and theoretical arguments (e.g., Fear et al., 2019) have suggested that FTEs at Mercury could make a much more significant contribution to the global Dungey cycle compared to the situation at Earth. Here we assess the importance of FTEs in contributing to the global circulation of magnetic flux in our simulations. In this analysis, we use the cross polar cap potential (CPCP) as a measure of the solar wind-magnetosphere coupling

Table 3

Comparison of Simulated Flux Transfer Event (FTE) Properties for Different Solar Wind M_A and Interplanetary Magnetic Field Clock Angles

FTE properties	Upstream conditions					
	$M_A = 6$			$M_A = 2$		
	Clock angle 180° (Run #1)	Clock angle 135° (Run #2)	Clock angle 90° (Run #3)	Clock angle 180° (Run #4)	Clock angle 135° (Run #5)	Clock angle 90° (Run #6)
Simulation duration	176 s	178 s	200 s	175 s	159 s	158 s
Total number of FTEs	52	42	23	68	60	49
Average occurrence rate	1 FTE every 3.4 s	1 FTE every 4.2 s	1 FTE every 8.7 s	1 FTE every 2.6 s	1 FTE every 2.7 s	1 FTE every 3.2 s
Average size	746 km	772 km	920 km	673 km	587 km	1002 km
Average speed	253 km/s	200 km/s	126 km/s	360 km/s	304 km/s	326 km/s
Average core field	46 nT	100 nT	110 nT	77 nT	170 nT	94 nT
Average flux content	0.005 MWb	0.016 MWb	0.025 MWb	0.010 MWb	0.030 MWb	0.028 MWb
Cross Polar Cap Potential	57 kV	50 kV	28 kV	119 kV	106 kV	69 kV
FTE contribution to open flux circulation	2.7%	7.5%	10.4%	3.1%	10.6%	12.7%

through magnetopause reconnection. The CPCP is calculated using the same approach described in detail by Zhou et al. (2020) from the simulation by integrating the convectional electric field along the dawn-to-dusk direction between the boundary points of the polar cap in the terminator plane. As discussed in Zhou et al. (2020), the CPCP calculated in this manner essentially can be viewed, as an approximation, the amount of magnetic flux per unit time opened through dayside magnetopause reconnection. We have verified that CPCP values are the same for the northern and southern hemispheres in our simulations, which is expected considering conservation of magnetic flux. However, it is worth noting that the northern and southern polar caps differ significantly in their size and shape because of the northward offset of Mercury's internal dipole.

With the statistics introduced previously on FTE occurrence rate and the average amount of magnetic flux carried by individual FTEs, we can evaluate the overall contribution of FTEs (C) to open flux generation on the dayside as follows:

$$C = \frac{\Phi_{\text{avg}} * N_{\text{FTE}}}{\text{CPCP} * T} \quad (9)$$

where Φ_{avg} is the average FTE open flux content presented in Figures 10–12, N_{FTE} is the total number of identified FTEs within the duration T of the simulation output that has been used in our statistical analysis. The results of CPCP and estimated contribution of FTEs to open flux generation are presented in the last two rows of Table 3 for all six simulations. For the various external conditions used in the simulation, the CPCP ranges between 28 and 119 kV, representing nominal and strong solar wind driving cases. The CPCP is found to increase with increasing IMF clock angle and decreasing solar wind M_A , which is consistent with the expectation based on how the reconnection rate depends on the upstream Alfvén speed and the shear angle across the magnetopause. As shown by the bottom row of Table 3, FTEs contribute about 3%–13% of the total magnetic flux opened through dayside reconnection for the upstream conditions considered in our study. These values indicate that FTEs at Mercury carry a significant portion of the open flux that participates in the Dungey cycle, which is in line with the finding reached in previous studies based on MESSENGER observations (e.g., Imber et al., 2014; J. A. Slavin et al., 2012; W. J. Sun et al., 2020b). Our simulation also reveals that the percentage contribution of FTEs to open flux generation increases with decreasing IMF clock angle, whereas it increases with decreasing solar wind M_A although the dependence on M_A is relatively weak compared to that on clock angle. The trend seen in the overall contribution of FTEs to the dayside open flux generation as function of IMF clock angle may imply that under large IMF clock angle conditions, more open flux is generated through single X-line reconnection, instead of multiple X-line reconnection that produces FTEs.

4. Discussion

In Section 3, we have presented the techniques used to identify FTEs from the various simulations and the properties of simulated FTEs extracted using those techniques. Here we summarize the key statistics of simulated FTEs

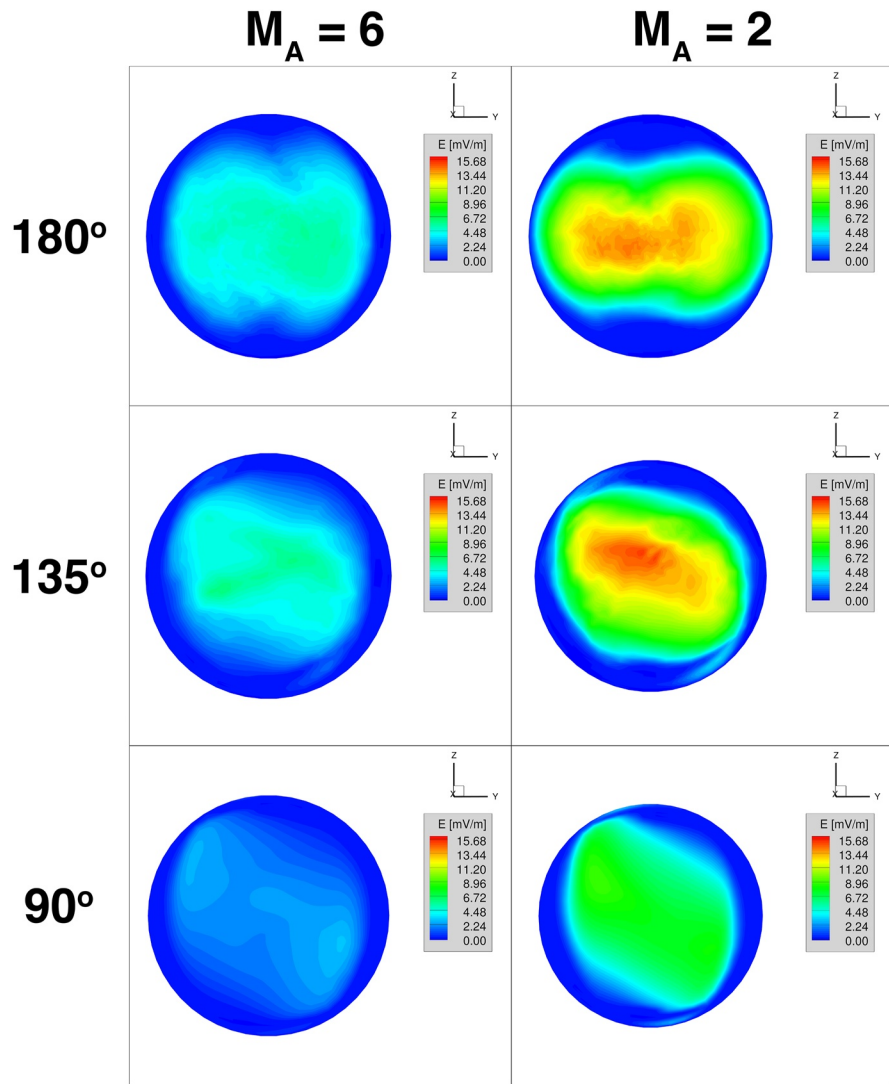


Figure 13. Time-averaged reconnection electric field on the magnetopause for the six simulations. The electric field is calculated according to the formula proposed by P. A. Cassak and Shay (2007) for asymmetric reconnection using the plasma and magnetic field conditions extracted on the magnetospheric and magnetosheath sides of the simulation, and then averaged over all timesteps to show the large-scale structure. The results are shown as contours projected onto the dayside magnetopause surface as viewed from the Sun.

in Table 3 for all six simulations. To obtain a better understanding of how the characteristics of FTEs depend on the upstream conditions, we have also evaluated the reconnection geometry and intensity at the magnetopause in order to place our FTE results into context. The main parameter of interest here is the reconnection electric field (E_{rec}), which can be estimated according to the following formula proposed by P. A. Cassak and Shay (2007) for asymmetric reconnection.

$$E_{\text{rec}} = 2kV_{\text{out}} \left(\frac{B_{\text{msh}} B_{\text{msp}}}{B_{\text{msh}} + B_{\text{msp}}} \right) \quad (10)$$

Here, B_{msh} and B_{msp} represent the reconnecting magnetic field component on the magnetosheath and magnetospheric side adjacent to the magnetopause boundary, respectively. k is the dimensionless reconnection rate, which is related to the aspect ratio of the diffusion region. Numerous previous studies have attempted to determine k for various reconnection scenarios in space plasmas and the commonly found order-of-magnitude value

for k is 0.1 (e.g., P. Cassak et al., 2017; Liu et al., 2017; W. J. Sun et al., 2020a), which is assumed in our calculation. V_{out} in the equation for E_{rec} represents the reconnection outflow flow speed, which can be obtained as follows:

$$V_{\text{out}} = \left[\frac{B_{\text{msh}} B_{\text{msp}} (B_{\text{msh}} + B_{\text{msp}})}{\mu_0 (\rho_{\text{msp}} B_{\text{msh}} + \rho_{\text{msh}} B_{\text{msp}})} \right]^{\frac{1}{2}}, \quad (11)$$

where ρ_{msh} and ρ_{msp} are the plasma mass density on the magnetosheath and magnetospheric side adjacent to the magnetopause boundary, respectively. Clearly, calculation of E_{rec} requires knowledge of the plasma and magnetic field conditions on both sides of the magnetopause boundary, which we extract from the simulation using a similar approach as used for identifying FTEs. After having determined the magnetopause surface based on the *Shue et al.* empirical model for each timestep, we scale the fitted magnetopause surface radially inward into magnetosphere and outward into magnetosheath by multiplying the previously determined “ r_0 ” parameter in Equation 8 with a coefficient of 0.9 and 1.1, respectively. The plasma density and magnetic field are then extracted from these two surfaces to calculate V_{out} and E_{rec} according to the equations above. Note that in this procedure we have to first determine from the extracted magnetic field vectors the reconnecting components between the magnetospheric and magnetosheath magnetic fields, which are the components that are anti-parallel to each other. The reconnection electric field is calculated for each timestep from the simulation and the mean electric field strength, which is averaged over all timesteps, is projected onto the magnetopause surface in Figure 13 to illustrate the large-scale geometry and intensity of the dayside magnetopause reconnection. It should be pointed out that the onset conditions for reconnection were not evaluated in this analysis, and our intention with estimating E_{rec} is to investigate how strong the reconnection electric field would be in each simulation using a different set of upstream conditions when reconnection occurs on the magnetopause. It is clear from Figure 13 that the reconnection electric field varies systematically in its strength and spatial distribution in response to changes in the external conditions. In particular, the overall strength of E_{rec} increases with decreasing solar wind M_A and increasing IMF clock angle, consistent with the expectation that these two parameters primarily control the Alfvén speed in the reconnection inflow region and the magnetic shear across the magnetopause boundary. The region where strong reconnection electric fields are present in each simulation, which can be deemed as a proxy for identifying the location of the primary X-line on the magnetopause, correlates closely with the IMF orientation imposed. For instance, the strongest $|E_{\text{rec}}|$ is concentrated in a horizontal belt near the magnetic equator in the 180° IMF clock angle simulations, whereas similar belts containing strong $|E_{\text{rec}}|$ are also present in the 135° and 90° IMF clock angle simulations but are tilted relative to the equatorial plane. The tilt angle is roughly 22.5° for the 135° cases and 45° for the 90° cases, which explains our choices of the “ θ_{FTE} ” parameter in the estimation of the FTE size and core field presented in Section 3.3.

With the results on the reconnection electric field as a global context, we now return to Table 3 to further discuss some of the general trends of our simulation results. We first examine the effects of solar wind M_A on FTEs by comparing each pair of columns color-coded with the same color in Table 3, for which the only difference between the simulations is the upstream solar wind M_A . For all three IMF orientations tested in our experiment, the occurrence rate of FTEs is consistently higher for $M_A = 2$ than for $M_A = 6$, which is in agreement with the MESSENGER observations reported by W. J. Sun et al. (2020). The more frequent FTE occurrence in lower M_A cases is a direct result of the enhanced reconnection electric field with decreasing solar wind M_A , as shown in Figure 13. Similarly, there is also a consistent trend in the average FTE traveling speed between different M_A simulations using the same IMF clock angle. That is the average speed increases with decreasing solar wind M_A , which, as we discussed previously, arises from the dependence of the reconnection outflow speed on the Alfvén speed in the reconnection inflow region. The other properties of FTEs appear to show somewhat different trends for different IMF clock angles. For example, for 180 and 135° clock angles, the average FTE size decreases by 10%–25% between $M_A = 6$ and $M_A = 2$ simulations, whereas it increases by ~10% for 90° IMF clock angle. Similarly, the average FTE core field increases significantly by ~70% when M_A decreases from 6 to 2 for 180 and 135° clock angle simulations, while it shows a slight decrease (~15%) for 90° clock angle simulations. Nonetheless, the average magnetic flux carried by FTEs consistently shows an increase with decreasing solar wind M_A for all IMF clock angles, although the relative increase is much larger for 180 and 135° cases than for 90° case.

Next, we examine the effects of the IMF orientation on the simulated FTE properties. The occurrence rate of FTEs increases monotonically with the IMF clock shear angle for both sets of simulations using the same solar

wind M_A . This result is consistent with the trend identified in the MESSENGER observations of FTEs (W. J. Sun et al., 2020b). The average FTE size in the latitudinal direction is comparable between the 180 and 135° cases, whereas it is significantly larger under 90° IMF clock angle conditions. Because the latitudinal scale lengths of FTEs largely depend on the spacing between neighboring reconnection X -lines, the size difference among different clock angle simulations can be partially attributed to the reconnection electric field shown in Figure 13. For 180 and 135° clock angles, both the average reconnection electric field strength (Figure 13) and the resultant CPCP (Table 3) are comparable to each other, while the reconnection electric field strength and CPCP become significantly smaller for 90° simulations.

Finally, we discuss the CPCP values determined for our simulations in comparison to prior work based on in-situ observations. As shown in Table 3, the CPCP in our simulations ranges from 28 to 119 kV, representing nominal and strong solar wind driving conditions used in the model. Various previous studies have estimated the CPCP based on MESSENGER data. For example, J. A. Slavin et al. (2009) estimated that the CPCP of Mercury's magnetosphere during MESSENGER's second close flyby (M2), which corresponds to nominal solar wind driving conditions, is around 30 kV. A subsequent work by DiBraccio et al. (2015) showed similar values (23 and 29 kV) from two plasma mantle case studies. W. J. Sun et al. (2020) analyzed stronger solar wind driving cases and found that the CPCP during the impact of a coronal mass ejection could increase to ~ 45 kV. While the CPCP values seen in our $M_A = 6$ simulations (28–57 kV) are in line with the range of CPCPs inferred by the previous observational work, the CPCP in our $M_A = 2$ simulations are significantly higher (69–119 kV), which deserves further discussion. It is important to note that the IMF field strength we chose for the $M_A = 2$ simulations is 69 nT, which is larger than the high end (~ 45 nT) of the range of IMF strengths typically observed at Mercury (W. Sun et al., 2022). As a result, stronger reconnection electric field and consequently larger CPCP are expected in the simulation. Therefore, the large CPCP values seen in the $M_A = 2$ simulations can be attributed in part to the relative strong IMF used in driving our simulation. To confirm if this is the case, we have also estimated the CPCP values analytically following the method adopted by W. Sun et al. (2022) based on the formula first proposed by Kivelson and Ridley (2008) (their Equation 13) for explaining the CPCP saturation phenomenon at Earth.

$$\text{CPCP} = 10^{-7} u_x^2 + 0.1\pi R_{\text{mp}} B_{\text{sw,yz}} u_x \sin^2\left(\frac{\theta}{2}\right) \frac{2\Sigma_A}{(\Sigma_A + \Sigma_p)}, \quad (12)$$

where u_x is the solar wind speed in m/s, R_{mp} is the subsolar magnetopause standoff distance in m , $B_{\text{sw,yz}}$ is the magnitude of the IMF component (in T) in the YZ plane, and Σ_A and Σ_p are the Alfvén conductance (in S) of the solar wind and the Pedersen conductance (in S) of the conducting region associated with the planet. As shown above, the formula to calculate CPCP requires knowledge of the upstream solar wind (u_x) and IMF ($B_{\text{sw,yz}}$) conditions, all of which are known as input parameters in our simulations, as well as the length of the reconnection X -line at the dayside magnetopause, for which we follow the typical assumption of using “ $0.1\pi R_{\text{mp}}$ ” as an approximation (R_{mp} is determined directly from the simulation by taking the average of r_0 in Equation 8 over all time-steps). Furthermore, the calculation also needs to know the Alfvén conductance of the solar wind $\Sigma_A = 1/(\mu_0 v_A)$, where v_A is the Alfvén speed in the upstream solar wind and μ_0 is the magnetic permeability in free space, as well as the Pedersen conductance (Σ_p) associated with any conductive region the planet may possess near its surface. Since Mercury lacks an appreciable ionosphere, the Pedersen conductance (Σ_p) can be deemed as the effective conductance in the planetary mantle (the layer immediately below the surface). Using the resistivity profile assumed in our simulations (e.g., Jia et al., 2015, 2019), we obtain $\Sigma_p \sim 0.05$ S, which is negligible compared to the Alfvén conductance (Σ_A) of the solar wind (of the order of a few S). Considering the 180° IMF clock angle cases as an example, putting the upstream conditions and the R_{mp} extracted from the simulation into Equation 12 yields a CPCP of 50 kV for $M_A = 6$ and 94 kV for $M_A = 2$. It can be seen that the CPCP values determined for our simulations are quite consistent with the theoretical predictions, which suggests that the seemingly high CPCPs seen in the $M_A = 2$ cases are most likely due to the stronger-than-typical IMF used in the model.

5. Summary and Conclusions

Motivated by the extensive observations of Mercury's magnetopause dynamics from MESSENGER, we have carried out a simulation study to investigate how the formation of FTEs and their contribution to the global dynamics are affected by external conditions. In this work, we employ the BATSRUS Hall MHD model (Tóth et al., 2008) with coupled planetary interior (Jia et al., 2015, 2019) to simulate Mercury's magnetosphere and

use a high-resolution grid with resolution of ~ 20 km (or $0.008 R_M$) near the magnetopause to well resolve the Hall effect that enables fast reconnection in the global simulation. A series of six global Hall MHD simulations have been conducted by using different sets of idealized upstream conditions designed to represent a range of solar wind and IMF conditions that could potentially be experienced by Mercury. The main external parameters of interest in this study are the solar wind Alfvénic Mach number and the IMF clock angle, for which several representative values ($M_A = 2$ and 6 , IMF clock angle = 90° , 135° , 180°) were chosen for our numerical experiment.

In all simulations, which were driven by fixed upstream conditions, Mercury's magnetopause reconnection is found to occur in a non-steady fashion resulting in FTEs with rope-like magnetic topology. To identify the large number of FTEs in the simulations, we have developed an automated algorithm that takes into consideration key characteristics of FTEs, such as the bi-polar variation of B_n associated with flux ropes. Important properties of FTEs, including their occurrence rate, size, traveling speed, core field strength and magnetic flux content, and their time histories were then extracted from all simulations and compared among different simulations to gain insight into the control of FTE properties by the solar wind. Below we summarize the key findings from our analysis.

FTEs are found to form frequently in all of the Mercury simulations with a new FTE born every 3–9 s for the external conditions used. The FTE occurrence rate shows a clear dependence on the solar wind M_A and the IMF orientation. Smaller solar wind M_A or larger IMF clock angle leads to more frequent occurrence of FTE. Both the range of FTE occurrence rate and its dependence on the upstream conditions are consistent with the results reported in the recent MESSENGER survey of FTE shower events at Mercury (W. J. Sun et al., 2020b).

FTEs formed in the simulations have a wide range of sizes, from <100 to ~ 2000 km. As FTEs evolve in time, their sizes also change due to their interaction with the surrounding plasma and magnetic field. In comparing the results from different simulations, we find that the average FTE size is comparable between 180° and 135° IMF clock angle cases, while FTEs in the 90° IMF clock angle cases have significantly larger size. A smaller solar wind M_A typically results in FTEs with smaller size under 180° and 135° IMF clock angle conditions, while producing FTEs with larger size under 90° IMF clock angle conditions.

By tracking the time history of FTE locations, we have also determined the traveling speeds of identified FTEs. FTEs formed in our simulations typically travel at speeds ranging between 200 and 400 km/s, which is close to the value previously assumed in various MESSENGER data analysis of FTEs. It is also found that the average FTE traveling speed generally becomes higher in lower solar wind M_A cases and in larger IMF clock angle cases. Such dependencies are consistent with the expectation of how reconnection outflow speed varies depending on the inflow Alfvén speed and magnetic shear angle at the magnetopause. The motion of FTEs is also significantly affected by the interplay between the geometry of magnetopause reconnection and large-scale plasma flows near the magnetopause.

The average core fields of FTEs seen in the simulations have a range from 50 to 170 nT for the external conditions used in this study, and the average magnetic flux content associated with FTEs falls in the range of 0.005–0.03 MWb. Overall, we find that individual FTEs normally carry more magnetic flux when the IMF clock angle is smaller or when the solar wind M_A is smaller. By comparing the aggregate magnetic flux carried by FTEs with the CPCP, which provides a measure of the global coupling efficiency, we find that FTEs contribute about 3%–13% of the open flux created at the dayside magnetopause that eventually participates in the global circulation of magnetic flux. This result is in general agreement with the previous findings obtained through analysis of MESSENGER data that FTEs at the magnetopause play a significant role in driving the Dungey cycle at Mercury.

In this work, we have used a global Hall MHD model to simulate Mercury's magnetopause dynamics focusing on the generation and evolution of FTEs under different external conditions. The main characteristics of our simulated FTEs agree generally well with the observations of FTEs by the MESSENGER spacecraft. In addition to confirming many of the previous observational findings, our simulations provide further insight into the 3D structure and motion of FTEs and how FTE properties are influenced by the solar wind and IMF. Our model results should provide useful context for interpreting in situ observations of Mercury's magnetosphere from spacecraft missions, such as MESSENGER and Bepi-Colombo, which is currently en route to Mercury with a scheduled arrival time of late 2025 (Millilo et al., 2020). The external parameters we have focused on in this paper are the solar wind Alfvénic Mach number and the IMF orientation. Future work to explore the influence of other external parameters in a broader parameter space, such as larger ranges of solar wind plasma parameters

(e.g., density and speed) and more realistic IMF conditions (e.g., inclusion of non-zero B_x component), may prove useful in order to obtain a more complete understanding of FTE formation and their role in driving global dynamics.

Data Availability Statement

The BATSRUS MHD code is publicly available for download as a component of the Space Weather Modeling Framework at the University of Michigan (<http://clasp.engin.umich.edu/swmf>).

Acknowledgments

This work was supported by NASA Future Investigators in Earth and Space Science and Technology (FINESST) Grant 80NSSC1364, NASA Early Career Fellow startup Grant 80NSSC20K1286, and NASA Discovery Data Analysis Program through Grant 80NSSC21K1012. J.A. Slavin acknowledges support from NASA Grant 80NSSC21K0052. G. Toth was supported by the NSF PREEVENTS Grant 1663800. High-performance computing resources supporting this work were provided by NASA's High-End Computing Program through its Advanced Supercomputing (NAS) Division at Ames Research Center.

References

- Anderson, B. J., Johnson, C. L., Korth, H., Purucker, M. E., Winslow, R. M., Slavin, J. A., et al. (2011). The global magnetic field of Mercury from MESSENGER orbital observations. *Science*, *333*(6051), 1859–1862. <https://doi.org/10.1126/science.1211001>
- Baker, D. N., Pulkkinen, T. I., Angelopoulos, V., Baumjohann, W., & McPherron, R. L. (1996). Neutral line model of substorms: Past results and present view. *Journal of Geophysical Research*, *101*(A6), 12975–13010. <https://doi.org/10.1029/95JA03753>
- Birn, J., Drake, J., Shay, M., Rogers, B., Denton, R., Hesse, M., et al. (2001). Geospace Environmental Modeling (GEM) magnetic reconnection challenge. *Journal of Geophysical Research*, *106*(A3), 3715–3719. <https://doi.org/10.1029/1999JA900449>
- Cassak, P., Liu, Y., & Shay, M. (2017). A review of the 0.1 reconnection rate problem. *Journal of Plasma Physics*, *83*(5), 715830501. <https://doi.org/10.1017/S0022377817000666>
- Cassak, P. A., & Shay, M. A. (2007). Scaling of asymmetric magnetic reconnection: General theory and collisional simulations. *Physics of Plasmas*, *14*(10), 102114. <https://doi.org/10.1063/1.2795630>
- Chen, Y., Tóth, G., Jia, X., Slavin, J. A., Sun, W., Markidis, S., et al. (2019). Studying dawn-dusk asymmetries of Mercury's magnetotail using MHD-EPIC simulations. *Journal of Geophysical Research: Space Physics*, *124*(11), 8954–8973. <https://doi.org/10.1029/2019JA026840>
- DiBraccio, G. A., Slavin, J. A., Boardsen, S. A., Anderson, B. J., Korth, H., Zurbuchen, T. H., et al. (2013). MESSENGER observations of magnetopause structure and dynamics at Mercury. *Journal of Geophysical Research: Space Physics*, *118*(3), 997–1008. <https://doi.org/10.1002/jgra.50123>
- DiBraccio, G. A., Slavin, J. A., Raines, J. M., Gershman, D. J., Tracy, P. J., Boardsen, S. A., et al. (2015). First observations of Mercury's plasma mantle by MESSENGER. *Geophysical Research Letters*, *42*(22), 9666–9675. <https://doi.org/10.1002/2015GL065805>
- Einfeldt, B., Munz, C. D., Roe, P. L., & Sjögreen, B. (1991). On Godunov-type methods near low densities. *Journal of Computational Physics*, *92*(2), 273–295. [https://doi.org/10.1016/0021-9991\(91\)90211-3](https://doi.org/10.1016/0021-9991(91)90211-3)
- Exner, W., Heyner, D., Liuzzo, L., Motschmann, U., Shiota, D., Kusano, K., & Shibayama, T. (2018). Coronal mass ejection hits Mercury: A.I.K.E.F. hybrid-code results compared to MESSENGER data. *Planetary and Space Science*, *153*, 89–99. <https://doi.org/10.1016/j.pss.2017.12.016>
- Fatemi, S., Poirier, N., Holmström, M., Lindkvist, J., Wieser, M., & Barabash, S. (2018). A modelling approach to infer the solar wind dynamic pressure from magnetic field observations inside Mercury's magnetosphere. *Astronomy & Astrophysics*, *614*, A132. <https://doi.org/10.1051/0004-6361/201832764>
- Fear, R. C., Coxon, J. C., & Jackman, C. M. (2019). The contribution of flux transfer events to Mercury's Dungey cycle. *Geophysical Research Letters*, *46*(24), 14239–14246. <https://doi.org/10.1029/2019GL085399>
- Gombosi, T. I., Chen, Y., Glocer, A., Huang, Z., Jia, X., Liemohn, M. W., et al. (2021). What sustained multi-disciplinary research can achieve: The space weather modeling framework. *Journal of Space Weather and Space Climate*, *11*, 42. <https://doi.org/10.1051/swsc/2021020>
- Heyner, D., Nabert, C., Liebert, E., & Glassmeier, K. H. (2016). Concerning reconnection-induction balance at the magnetopause of Mercury. *Journal of Geophysical Research: Space Physics*, *121*(4), 2935–2961. <https://doi.org/10.1002/2015JA021484>
- Imber, S. M., Slavin, J. A., Boardsen, S. A., Anderson, B. J., Korth, H., McNutt, R. L., & Solomon, S. C. (2014). MESSENGER observations of large dayside flux transfer events: Do they drive Mercury's substorm cycle? *Journal of Geophysical Research: Space Physics*, *119*(7), 5613–5623. <https://doi.org/10.1002/2014JA019884>
- Jia, X., Slavin, J. A., Gombosi, T. I., Daldorff, L. K. S., Toth, G., & van der Holst, B. (2015). Global MHD simulations of Mercury's magnetosphere with coupled planetary interior: Induction effect of the planetary conducting core on the global interaction. *Journal of Geophysical Research: Space Physics*, *120*(6), 4763–4775. <https://doi.org/10.1002/2015JA021143>
- Jia, X., Slavin, J. A., Poh, G., DiBraccio, G. A., Toth, G., Chen, Y., et al. (2019). MESSENGER observations and global simulations of highly compressed magnetosphere events at Mercury. *Journal of Geophysical Research: Space Physics*, *124*(1), 229–247. <https://doi.org/10.1029/2018JA026166>
- Kabin, K., Heimpel, M. H., Rankin, R., Aurnou, J. M., Gómez-Pérez, N., Paral, J., et al. (2008). Global MHD modeling of Mercury's magnetosphere with applications to the MESSENGER mission and dynamo theory. *Icarus*, *195*, 1–15. <https://doi.org/10.1016/j.icarus.2007.11.028>
- Kieokaeuw, R., Lavraud, B., Fargette, N., Marchaudon, A., Génot, V., Jacquy, C., et al. (2021). Statistical relationship between interplanetary magnetic field conditions and the helicity sign of flux transfer event flux ropes. *Geophysical Research Letters*, *48*(6), e2020GL091257. <https://doi.org/10.1029/2020GL091257>
- Kivelson, M. G., & Ridley, A. J. (2008). Saturation of the polar cap potential: Inference from Alfvén wing arguments. *Journal of Geophysical Research*, *113*(A5), A05214. <https://doi.org/10.1029/2007JA012302>
- Koren, B. (1993). *A robust upwind discretization method for advection, diffusion and source terms*. Centrum voor Wiskunde en Informatica Amsterdam.
- Kuznetsova, M. M., Sibeck, D. G., Hesse, M., Wang, Y., Rastaetter, L., Toth, G., & Ridley, A. (2009). Cavities of weak magnetic field strength in the wake of FTEs: Results from global magnetospheric MHD simulations. *Geophysical Research Letters*, *36*(10), L10104. <https://doi.org/10.1029/2009GL037489>
- Lapenta, G., Schriver, D., Walker, R. J., Berchem, J., Echterling, N. F., El Alaoui, M., & Travnicek, P. (2022). Do we need to consider electrons' kinetic effects to properly model a planetary magnetosphere: The case of Mercury. *Journal of Geophysical Research: Space Physics*, *127*(4), e2021JA030241. <https://doi.org/10.1029/2021JA030241>
- Lavorenti, F., Henri, P., Califano, F., Deca, J., Aizawa, S., André, N., & Benkhoff, J. (2022). Electron dynamics in small magnetospheres—Insights from global, fully kinetic plasma simulations of the planet Mercury. *Astronomy & Astrophysics*, *664*, A133. <https://doi.org/10.1051/0004-6361/202243911>

- Liu, Y.-H., Cassak, P., Li, X., Hesse, M., Lin, S.-C., & Genestreti, K. (2022). First-principles theory of the rate of magnetic reconnection in magnetospheric and solar plasmas. *Communications Physics*, 5(1), 97. <https://doi.org/10.1038/s42005-022-00854-x>
- Liu, Y.-H., Hesse, M., Guo, F., Daughton, W., Li, H., Cassak, P., & Shay, M. (2017). Why does steady-state magnetic reconnection have a maximum local rate of order 0.1? *Physical Review Letters*, 118(8), 085101. <https://doi.org/10.1103/PhysRevLett.118.085101>
- Lu, Q., Guo, J., Lu, S., Wang, X., Slavin, J. A., Sun, W., et al. (2022). Three-dimensional global hybrid simulations of flux transfer event showers at Mercury. *The Astrophysical Journal*, 937(1), 1. <https://doi.org/10.3847/1538-4357/ac8bcf>
- Millilo, A., Fujimoto, M., Murakami, G., Benkhoff, J., Zender, J., Aizawa, S., et al. (2020). Investigating Mercury's environment with the two-spacecraft BepiColombo mission. *Space Science Reviews*, 216, 1–78. <https://doi.org/10.1007/s11214-020-00712-8>
- Müller, J., Simon, S., Wang, Y. C., Motschmann, U., Heyner, D., Schüle, J., et al. (2012). Origin of Mercury's double magnetopause: 3D hybrid simulation study with A.I.K.E.F. *Icarus*, 218(1), 666–687. <https://doi.org/10.1016/j.icarus.2011.12.028>
- Powell, K. G., Roe, P. L., Linde, T. J., Gombosi, T. I., & De Zeeuw, D. L. (1999). A solution-adaptive upwind scheme for ideal magnetohydrodynamics. *Journal of Computational Physics*, 154(2), 284–309. <https://doi.org/10.1006/jcph.1999.6299>
- Raines, J. M., DiBraccio, G. A., Cassidy, T. A., Delcourt, D., Fujimoto, M., Jia, X., et al. (2015). Plasma sources in planetary magnetospheres: Mercury. *Space Science Reviews*, 192(1–4), 91–144. <https://doi.org/10.1007/s11214-015-0193-4>
- Russell, C. T., & Elphic, R. (1978). Initial ISEE magnetometer results: Magnetopause observations. *Space Science Reviews*, 22(6), 681–715. <https://doi.org/10.1007/BF00212619>
- Shue, J.-H., Chao, J. K., Fu, H. C., Russell, C. T., Song, P., Khurana, K. K., & Singer, H. J. (1997). A new functional form to study the solar wind control of the magnetopause size and shape. *Journal of Geophysical Research*, 102(A5), 9497–9511. <https://doi.org/10.1029/97JA00196>
- Slavin, J., Middleton, H., Raines, J., Jia, X., Zhong, J., Sun, W. J., et al. (2019). MESSENGER observations of disappearing dayside magnetosphere events at Mercury. *Journal of Geophysical Research: Space Physics*, 124(8), 6613–6635. <https://doi.org/10.1029/2019JA026892>
- Slavin, J. A., Acuña, M. H., Anderson, B. J., Baker, D. N., Benna, M., Boardsen, S. A., et al. (2009). MESSENGER observations of magnetic reconnection in Mercury's magnetosphere. *Science*, 324(5927), 606–610. <https://doi.org/10.1126/science.1172011>
- Slavin, J. A., Anderson, B. J., Baker, D. N., Benna, M., Boardsen, S. A., Gloeckler, G., et al. (2010). MESSENGER observations of extreme loading and unloading of Mercury's magnetic tail. *Science*, 329(5992), 665–668. <https://doi.org/10.1126/science.1188067>
- Slavin, J. A., Anderson, B. J., Baker, D. N., Benna, M., Boardsen, S. A., Gold, R. E., et al. (2012). MESSENGER and Mariner 10 flyby observations of magnetotail structure and dynamics at Mercury. *Journal of Geophysical Research*, 117(A1), 1215. <https://doi.org/10.1029/2011JA016900>
- Slavin, J. A., DiBraccio, G. A., Gershman, D. J., Imber, S. M., Poh, G. K., Raines, J. M., et al. (2014). MESSENGER observations of Mercury's dayside magnetosphere under extreme solar wind conditions. *Journal of Geophysical Research: Space Physics*, 119(10), 8087–8116. <https://doi.org/10.1002/2014JA020319>
- Slavin, J. A., & Holzer, R. E. (1979). The effect of erosion on the solar wind stand-off distance at Mercury. *Journal of Geophysical Research*, 84(A5), 2076–2082. <https://doi.org/10.1029/JA084iA05p02076>
- Sun, T. R., Tang, B. B., Wang, C., Guo, X. C., & Wang, Y. (2019). Large-scale characteristics of flux transfer events on the dayside magnetopause. *Journal of Geophysical Research: Space Physics*, 124, 2425–2434. <https://doi.org/10.1029/2018JA026395>
- Sun, W., Dewey, R. M., Aizawa, S., Huang, J., Slavin, J. A., Fu, S., et al. (2022a). Review of Mercury's dynamic magnetosphere: Post-MESSENGER era and comparative magnetospheres. *Science China Earth Sciences*, 65(1), 25–74. <https://doi.org/10.1007/s11430-021-9828-0>
- Sun, W., Slavin, J. A., Milillo, A., Dewey, R. M., Orsini, S., Jia, X., et al. (2022b). MESSENGER observations of planetary ion enhancements at Mercury's northern magnetospheric cusp during flux transfer event showers. *Journal of Geophysical Research: Space Physics*, 127(4), e2022JA030280. <https://doi.org/10.1029/2022JA030280>
- Sun, W. J., Slavin, J. A., Dewey, R. M., Chen, Y., DiBraccio, G. A., Raines, J. M., et al. (2020a). MESSENGER observations of Mercury's nightside magnetosphere under extreme solar wind conditions: Reconnection-generated structures and steady convection. *Journal of Geophysical Research: Space Physics*, 125(3), e2019JA027490. <https://doi.org/10.1029/2019JA027490>
- Sun, W. J., Slavin, J. A., Smith, A. W., Dewey, R. M., Poh, G. K., Jia, X., et al. (2020b). Flux transfer event showers at Mercury: Dependence on plasma β and magnetic shear and their contribution to the Dungey cycle. *Geophysical Research Letters*, 47(21), e2020GL089784. <https://doi.org/10.1029/2020GL089784>
- Tóth, G. (2000). The $\nabla \cdot \mathbf{B} = 0$ constraint in shock-capturing magnetohydrodynamics codes. *Journal of Computational Physics*, 161(2), 605–652. <https://doi.org/10.1006/jcph.2000.6519>
- Tóth, G., Chen, Y., Gombosi, T. I., Cassak, P., Markidis, S., & Peng, I. B. (2017). Scaling the ion inertial length and its implications for modeling reconnection in global simulations. *Journal of Geophysical Research: Space Physics*, 122(10), 10336–10355. <https://doi.org/10.1002/2017JA024189>
- Tóth, G., Ma, Y., & Gombosi, T. I. (2008). Hall magnetohydrodynamics on block-adaptive grids. *Journal of Computational Physics*, 227(14), 6967–6984. <https://doi.org/10.1016/j.jcp.2008.04.010>
- Tóth, G., Van der Holst, B., Sokolov, I. V., De Zeeuw, D. L., Gombosi, T. I., Fang, F., et al. (2012). Adaptive numerical algorithms in space weather modeling. *Journal of Computational Physics*, 231(3), 870–903. <https://doi.org/10.1016/j.jcp.2011.02.006>
- Trávníček, P. M., Schriver, D., Hellinger, P., Herčík, D., Anderson, B. J., Sarantos, M., & Slavin, J. A. (2010). Mercury's magnetosphere-solar wind interaction for northward and southward interplanetary magnetic field: Hybrid simulation results. *Icarus*, 209(1), 11–22. <https://doi.org/10.1016/j.icarus.2010.01.008>
- Winslow, R. M., Anderson, B. J., Johnson, C. L., Slavin, J. A., Korth, H., Purucker, M. E., et al. (2013). Mercury's magnetopause and bow shock from MESSENGER Magnetometer observations. *Journal of Geophysical Research: Space Physics*, 118(5), 2213–2227. <https://doi.org/10.1002/jgra.50237>
- Zhou, H., Toth, G., Jia, X., & Chen, Y. (2020). Reconnection-driven dynamics at Ganymede's upstream magnetosphere: 3-D global Hall MHD and MHD-EPIC simulations. *Journal of Geophysical Research: Space Physics*, 125(8), e2020JA028162. <https://doi.org/10.1029/2020JA028162>
- Zhou, H., Tóth, G., Jia, X., Chen, Y., & Markidis, S. (2019). Embedded kinetic simulation of Ganymede's magnetosphere: Improvements and inferences. *Journal of Geophysical Research: Space Physics*, 124(7), 5441–5460. <https://doi.org/10.1029/2019JA026643>